NASA/TM-20220015637

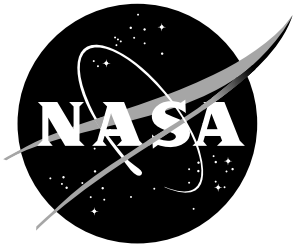

Experimental Validation of an Acoustically and Aerodynamically Optimized UAM Proprotor Part 1: Test Setup and Results

Nikolas S. Zawodny, Nicole A. Pettingill, Leonard V. Lopes
Langley Research Center, Hampton, Virginia

Daniel J. Ingraham
Glenn Research Center, Cleveland, Ohio

February 2023

NASA STI Program. . . in Profile

Since its founding, NASA has been dedicated to the advancement of aeronautics and space science. The NASA scientific and technical information (STI) program plays a key part in helping NASA maintain this important role.

The NASA STI Program operates under the auspices of the Agency Chief Information Officer. It collects, organizes, provides for archiving, and disseminates NASA's STI. The NASA STI Program provides access to the NASA Aeronautics and Space Database and its public interface, the NASA Technical Report Server, thus providing one of the largest collection of aeronautical and space science STI in the world. Results are published in both non-NASA channels and by NASA in the NASA STI Report Series, which includes the following report types:

- TECHNICAL PUBLICATION. Reports of completed research or a major significant phase of research that present the results of NASA programs and include extensive data or theoretical analysis. Includes compilations of significant scientific and technical data and information deemed to be of continuing reference value. NASA counterpart of peer-reviewed formal professional papers, but having less stringent limitations on manuscript length and extent of graphic presentations.
- TECHNICAL MEMORANDUM. Scientific and technical findings that are preliminary or of specialized interest, e.g., quick release reports, working papers, and bibliographies that contain minimal annotation. Does not contain extensive analysis.
- CONTRACTOR REPORT. Scientific and technical findings by NASA-sponsored contractors and grantees.
- CONFERENCE PUBLICATION. Collected papers from scientific and technical conferences, symposia, seminars, or other meetings sponsored or co-sponsored by NASA.
- SPECIAL PUBLICATION. Scientific, technical, or historical information from NASA programs, projects, and missions, often concerned with subjects having substantial public interest.
- TECHNICAL TRANSLATION. English-language translations of foreign scientific and technical material pertinent to NASA's mission.

Specialized services also include organizing and publishing research results, distributing specialized research announcements and feeds, providing information desk and personal search support, and enabling data exchange services.

For more information about the NASA STI Program, see the following:

- Access the NASA STI program home page at `http://www.sti.nasa.gov`
- E-mail your question to `help@sti.nasa.gov`
- Phone the NASA STI Information Desk at 757-864-9658
- Write to:
  NASA STI Information Desk
  Mail Stop 148
  NASA Langley Research Center
  Hampton, VA 23681-2199

NASA/TM–20220015637

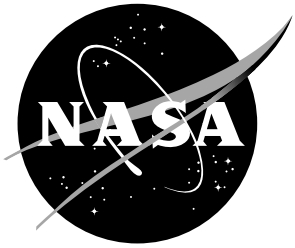

Experimental Validation of an Acoustically and Aerodynamically Optimized UAM Proprotor Part 1: Test Setup and Results

Nikolas S. Zawodny, Nicole A. Pettingill, Leonard V. Lopes
Langley Research Center, Hampton, Virginia

Daniel J. Ingraham
Glenn Research Center, Cleveland, Ohio

National Aeronautics and
Space Administration

Langley Research Center
Hampton, Virginia 23681-2199

February 2023

Acknowledgments

This work is funded by NASA's Aeronautics Research Mission Directorate (ARMD), specifically the Transformative Tools and Technologies (TTT) Project in the Transformative Aeronautics Concepts Program (TACP).

Available from:

NASA STI Program / Mail Stop 148
NASA Langley Research Center
Hampton, VA 23681-2199
Fax: 757-864-6500

Abstract

Vehicles with vectored thrust capabilities are common configurations proposed for Urban Air Mobility (UAM) flight missions. These include proprotor systems capable of vertical takeoff and landing (VTOL), axial forward flight, and the intermediate transition phases of vehicle flight. The aerodynamic loading requirements, as well as resulting acoustics, during these different phases of flight can vary considerably. An optimization effort was undertaken with the objective of minimizing radiated tonal acoustics of a proprotor system for both static hover and axial forward flight conditions, while simultaneously preserving aerodynamic performance relative to a baseline propeller design.

Contents

1 Introduction

Urban Air Mobility (UAM) aircraft are key components of the emerging Advanced Air Mobility (AAM) aviation industry. UAM aircraft are planned to perform passenger transport missions up to 120 km (75 miles) around metropolitan areas [1]. Vehicles capable of transitioning between VTOL and axial forward phases of flight, also known as vectored thrust vehicles, are very appealing to the AAM industry. This is partially because such vehicles do not require an airport or runway length typical of conventional fixed-wing aircraft. Another reason such vehicles are appealing to the AAM industry is that they are anticipated to be both quieter and more efficient than conventional VTOL vehicles, such as helicopters, during the cruise phases of flight.

One example of a UAM vectored thrust vehicle is the NASA tiltwing reference vehicle, designed under the Revolutionary Vertical Lift Technology (RVLT) project [2]. Illustrations of this vehicle concept are provided in Fig. 1. As discussed in Reference 2, the proprotors for this vehicle have dramatically different thrust requirements for the two phases of flight illustrated in Fig. 1. For example, Reference 2 documents a required proprotor disk loading of 20 lbf/ft^2 in hover, and a disk loading of only 1.88 lbf/ft^2 in axial cruise.

(a) VTOL mode (b) Axial forward flight mode

Figure 1. Visualizations of the NASA RVLT tiltwing reference vehicle concept in (a) VTOL and (b) axial forward flight phases of flight.

The wide range of disk loading conditions encountered by a vectored thrust vehicle, such as the tiltwing, prompted an aeroacoustic question: **Can a single proprotor be designed using adjoint optimization to satisfy an acoustic objective for a UAM vectored thrust vehicle configuration given a target set of hover and cruise flight conditions?** An adjoint optimization method is a computation that uses Lagrange multiplier forms of equations to provide the gradient of an objective function, which is used to iterate to minimize or maximize an objective while, optionally, meeting constraint criteria. In this study, the constraint criteria are the thrust and power at the prescribed flight conditions, and the objective function is the minimization of an overall sound pressure level (SPL). This report documents the experimental findings of several proprotors designed to satisfy such an objective function. Both the aerodynamic and acoustic performances of these proprotors are compared against those of a baseline propeller design, which served as the starting configuration from which the proprotor designs originated.

2 Computational Approach

The following sections discuss the technical approaches encompassing the computational design tools and methods. Two approaches were taken: a low-fidelity design approach and a high-fidelity design approach. In the following sections, the commonality between the approaches will be explained and, subsequently, details unique to each approach will be presented. Following the processes used in the study, the resultant blade designs will be shown.

2.1 Optimization Design Process

Regardless of the fidelity of the approach taken, certain parts of the design optimization process were similar. Figure 2 presents an Extended Design Structure Matrix (XDSM) that shows the connection between the aerodynamic, source noise prediction, and acoustic constraint components of the design process. Initial conditions were provided to an optimization block of the design process. The optimization block provided blade shape properties along with proprotor diameters, propeller D_{prop} and hub D_{hub}, and freestream velocities, v_∞, to the aerodynamic section of the optimization process. The aerodynamic process block provided performance properties (efficiency, η, and thrust, T) back to the optimizer to be used as either an objective or constraint in the optimization problem. In addition to the performance properties, blade loads were provided to the source noise component of the optimization process which also recieved the freestream velocities and observer positions, $\boldsymbol{x}_j$, where subscript j denotes observer position index. In the current studies, both high- and low-fidelity approaches utilized Farassat's Formulation 1A (F1A) as the source noise prediction component [3–5]. Acoustic pressure time histories (APTH) from the source noise computational block were provided to the acoustic constraint block, which computed the acoustic constraint, $\mathscr{L}$. The computed $\mathscr{L}$ was then provided back to the optimizer as a constraint. After the optimization process completed, optimized values were returned and are denoted by the superscript $*$ in Fig. 2.

The target hover and cruise operating conditions of the proprotors are defined in Table 1. As the table shows, the operating conditions are defined in terms of a thrust requirement for the two modes of flight and are based on the performance at these flight conditions for a constant tip speed condition at constant blade pitch. Using the diameter of the baseline propeller as the dimensional reference, the physical proprotor properties correspond to proprotor disk loadings in hover and cruise of 18.9 lbf/ft^2 and 7.6 lbf/ft^2, respectively. While the hover disk loading condition in Table 1 is closely representative of the tiltwing concept mentioned in Section 1, the cruise target condition is relatively high compared to the same tiltwing concepts. This is because of a combination of factors related to facility flow speed capabilities, signal-to-noise ratio concerns, and load cell measurement accuracy.

Overall, the goal of the optimizations was to design a blade that produced the same thrust as the baseline propeller, but was much quieter and as aerodynamically efficient as possible. Unique aspects of the low- and high-fidelity design process include the aerodynamic model, compactness assumption used in F1A, flight con-

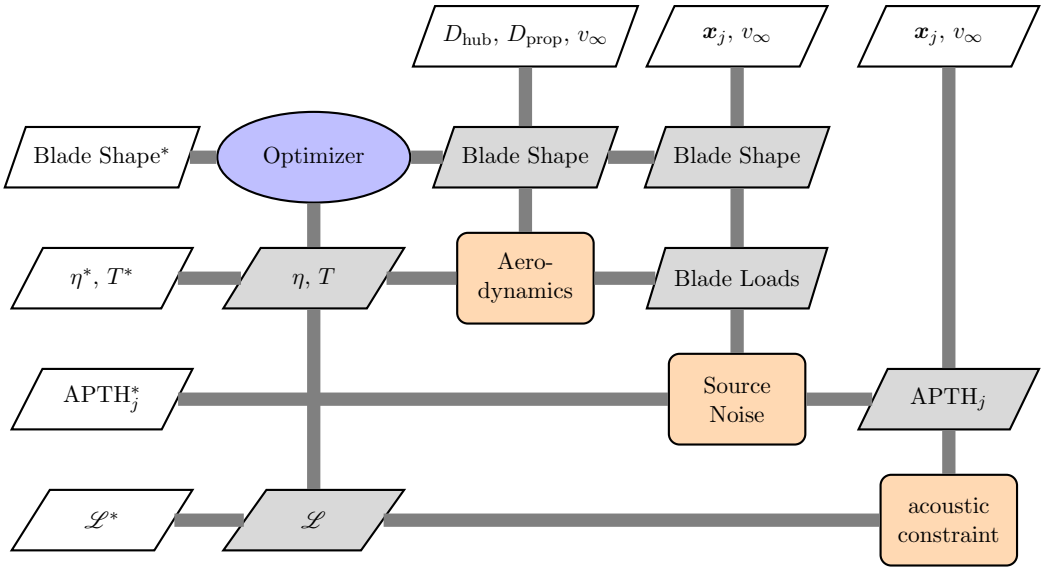

Figure 2. XDSM for isolated propeller rotor design.

Table 1. Proprotor thrust requirements for hover and cruise flight conditions.

Flight Condition	M_∞	Target Thrust (N, lb.)
Hover	0.00	264.5, 59.5
Cruise	0.11	106.5, 24.0

ditions, observer positions, and acoustic constraint metric. These will be presented in the following sections.

2.1.1 Low-fidelity Design Process

The aerodynamic component used in the low-fidelity approach was provided by CCBlade.jl, an implementation of blade element momentum theory (BEMT) especially well-suited to gradient-based optimization [6]. Blade element momentum theory (cf. chapter 3 of Leishman [7]) is a low-order approach to simulating propeller and proprotor aerodynamics. While not as capable as more sophisticated vortex-based methods or computational fluid dynamics (CFD), BEMT works quite well for isolated proprotors experiencing on-axis flow, and the computational efficiency of BEMT makes it especially attractive for preliminary design work (e.g., where a large number of designs are to be evaluated quickly), and highly multidisciplinary design optimizations (e.g., where the propeller aerodynamics are one small piece of a large computational model). The compact form of F1A, as implemented in the computer program AcousticAnalogies.jl, was used to reduce the surface integrals associated with the noncompact Formulation to line integrals along the blade span [8, 9]. This reduces the computational cost of the acoustic model, and also is quite convenient, as the loading per unit span calculated by the BEMT aerodynamic model can be fed directly to the compact F1A routine. In addition, only a single forward flight

propeller mode freestream velocity of $M = 0.11$ and a single in-plane observer position was analyzed during the optimization. Finally, overall sound pressure level (OASPL) was used as the acoustic constraint.

The aerodynamic, source noise, and acoustic constraint components of the optimization were linked together within the optimization framework OpenMDAO [10], which was then used to create and solve the following constrained optimization problem to design the proprotors:

- objective: maximize η, cruise efficiency
- design variables:
  - $c(r)$, chord distribution at eight spline control points
  - $\phi(r)$, twist distribution at eight spline control points
  - Ω, proprotor rotation speed
- constraints:
  - T, thrust at cruise
  - OASPL at a sideline microphone location at cruise

The thrust constraint was set to the value predicted by CCBlade.jl for a baseline proprotor design (the C24ND, discussed subsequently) at the cruise condition, while the OASPL constraint was set at a level x dB below what was found for an optimization identical to the one discussed above, but without the acoustic constraint, where $x == 2$ dB for a three-blade design (the COPR-3) and $x == 4$ dB for a five-blade design (the COPR-5). The sideline OASPL levels of the optimizations without the acoustic constraint were already quite a bit quieter than the C24ND, so a further noise reduction of 2 or 4 dB represents a significant decrease.

The SNOPT optimizer [11], called from OpenMDAO via the pyOptSparse [12] Python package, was used to solve the above optimization problem. To accelerate convergence of the optimization problem, gradients of the objective function and each constraint were calculated via the ForwardDiff.jl [13] automatic differentiation package and provided to the OpenMDAO framework and SNOPT. More details of the optimization process results were presented previously in Ref. [14] and will be the subject of a Part 2 of this technical memorandum.

2.1.2 High-fidelity Design Process

The aerodynamic component of the high-fidelity optimization utilitized the Stanford University Unstructured (SU2) CFD framework that includes an Unsteady Reynolds averaged Navier-Stokes (URANS) solver to analyze compressible, turbulent flows commonly found in aerospace engineering problems. The governing equations are spatially discretized using a finite volume method on unstructured grids, the time marching of the semidiscretized URANS equations is performed by a dual time-stepping method, and the Spalart-Allmaras (SA) turbulence model was used. The source noise component of the optimization process utilized the noncompact form

of Formulation 1A to predict APTH at multiple observer locations coinciding with the microphone locations defined in Chapter 3 for one hover and one forward flight configuration that coincides with that used in the low-fidelity computation. The acoustic constraint metric utilized not only the multiple observer locations and multiple flight conditions, but also A-weighted OASPL, which models the annoyance of the noise by weighting frequency content to which the human ear is most sensitive. The objective function for the high-fidelity optimization includes the multiple observer locations, multiple flight conditions, and human perception, and is shown in Eq. 1,

$$F = 10\log_{10}\left[\int_{\theta_{l,H}}^{\theta_{u,H}} \frac{\langle p^2\rangle_{A,H}}{\sin\theta} d\theta\right] + 10\log_{10}\left[\int_{\theta_{l,J}}^{\theta_{u,J}} \frac{\langle p^2\rangle_{A,J}}{\sin\theta} d\theta\right], \tag{1}$$

where subscripts A, H, and J denote A-weighting, hover condition, and forward flight condition, respectively, and θ is defined as 0° in the rotation axis direction. Also, in Eq. 1, the subscripts u and l denote upper and lower limits, respectively. Further details and references are cited in Ref.[15].

In contrast to the low-fidelity optimization process, two additional factors radically changed the design ultimately achieved by the optimization. The first is that SU2 had difficulty shrinking the blade tip; therefore, an additional constraint was enforced that limited the tip chord size. In addition, while the low-fidelity optimization parameterized the blade design that included radial definitions of twist and chord, SU2 utilized a free-form deformation (FFD) box. The FFD boxes and the parameterization of control points are shown in Fig. 3. The control points near trailing and leading edges move in the direction of red arrows to parametrize chord length. Moreover, middle control points move in the direction of the blue arrow to assess the cambered airfoil effects on the performance. Additionally, the tip region inward movement is controlled as shown with green arrows. Lastly, planes at each radial station manage the twist angle of airfoils by the given rotation inputs, denoted by the yellow arrows. Overall, optimization studies consist of 55 design variables using the Bezier-Bernstein polynomials for the deformations.

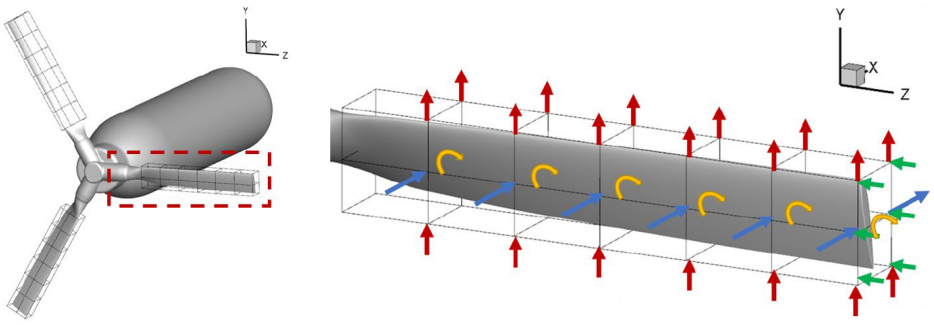

(a) (b)

Figure 3. (a) FFD boxes wrapping three blades of the proprotor and (b) parametrization of control points.

2.2 Proprotor Designs

The low- and high-fidelity optimization processes resulted in two blade designs that were used to fabricate three proprotor designs. With the baseline design, denoted C24ND, this resulted in four proprotor designs. The first optimized blade design was informed by the approach outlined in Sec. 2.1.2 and resulted in one three-bladed proprotor denoted Opt-III, and the second blade design using the approach outlined in Sec. 2.1.1 that resulted in a three-bladed proprotor, denoted the Computationally Optimized Proprotor (COPR-3), and a five-bladed version (COPR-5). Photographs of the proprotors tested in this investigation are provided in Fig. 4. Comparisons in blade chord and twist distributions between the different blade designs are provided in Fig. 5.

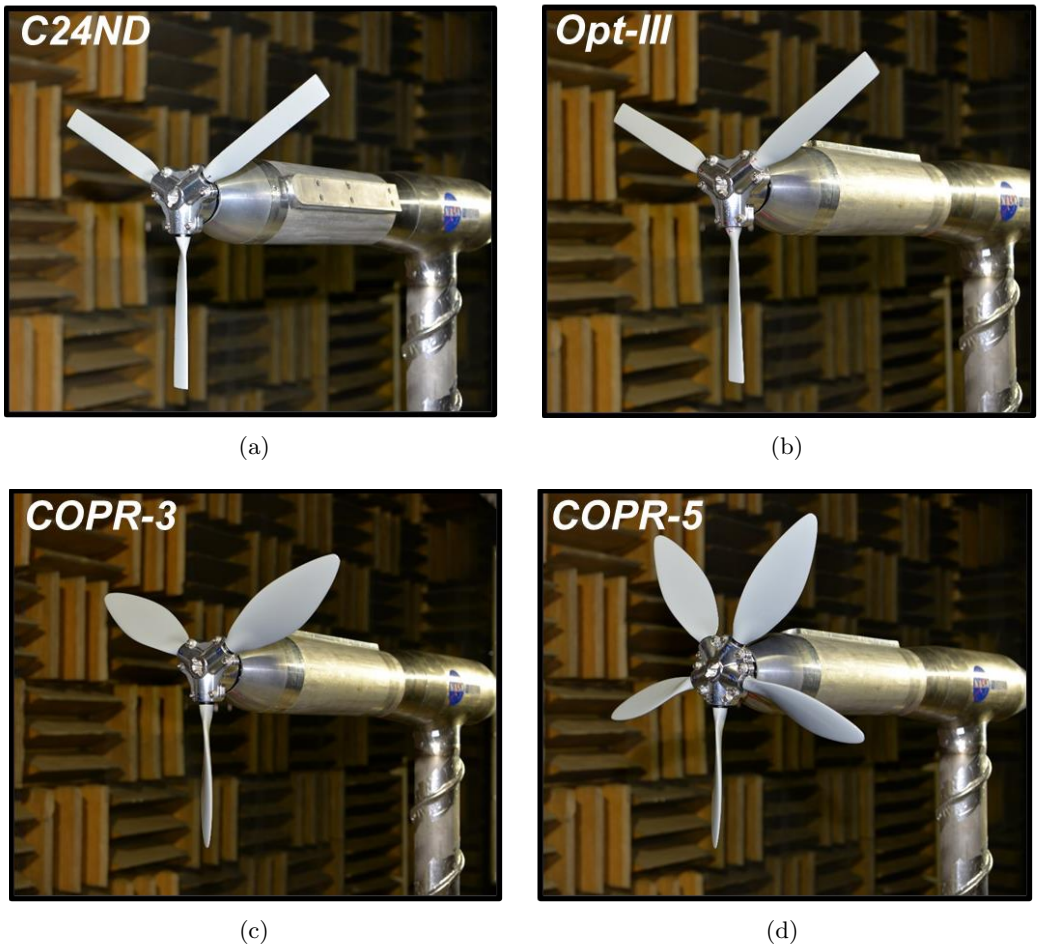

(a) (b)

(c) (d)

Figure 4. Photographs of the proprotor test articles: (a) helically-twisted propeller (C24ND), (b) CFD-based adjoint design (Opt-III), (c) three-bladed blade element theory optimized design (COPR-3), and (d) 5-bladed optimized design (COPR-5). [Source: NASA]

The C24ND propeller shown in Fig. 4(a) is a three-bladed helically twisted propeller with a constant spanwise chord distribution ($c = \text{const.}$), as well as a nomi-

nally spanwise constant NACA 0012 airfoil profile. The helical sweep distribution is defined as

$$\phi(r/R) = \tan^{-1}\left[\frac{P}{\pi D_p(r/R)}\right], \tag{2}$$

where $\phi(r/R)$ is the blade geometric twist angle at station r, P is the propeller pitch, D_p is the propeller diameter, and R is the propeller radius. The primary geometric parameters of the C24ND propeller are provided in Table 2. This propeller serves as the baseline input design for the implemented optimization routines.

Table 2. Geometric parameters for the C24ND propeller.

Parameter	Value
c, in. (mm)	1.5 (38.1)
P, in. (mm)	16.0 (406.4)
D_p, in. (mm)	24.0 (609.6)

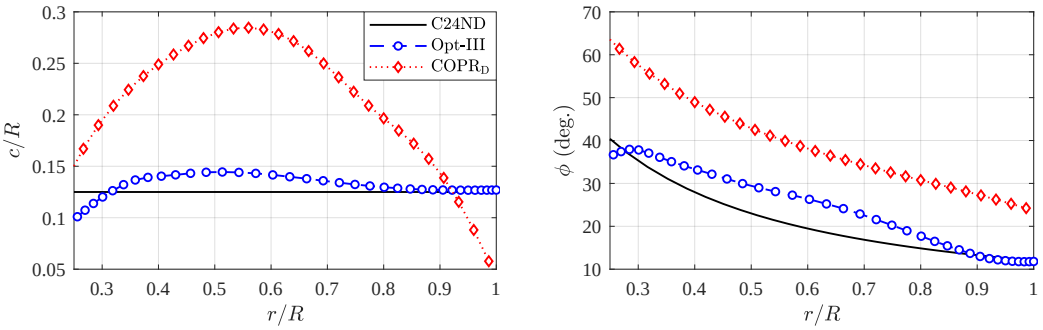

(a) Chord distributions

(b) Twist angle distributions

Figure 5. Comparison of blade (a) chord distributions and (b) twist angle distributions for the tested proprotors.

Figure 6 provides a profile comparison between the nominal design (D) for the COPR blade and the "as manufactured" (M) COPR blade. This figure is illustrative of the potential variability in a blade design in going from a design on paper to a final fabricated product. Figure 6(a) shows very close agreement between the two chord profiles, with a more uniform roll-off behavior in the manufactured blade across the spanwise range $0.65 \leq r/R \leq 0.85$. Figure 6(b) shows a nearly identical blade twist distribution between the two designs, with the exception of the angles over a range of $r/R \leq 0.35$. This region of the blade span represents one that was forced to deviate from the original design, allowing the blade to be properly fixtured into the proprotor hub structure. The duration of this document will be analyzing the manufactured blade, and will herein simply be referred to as the COPR blade.

It is important to note that a fundamental difference in the operating conditions of the Opt-III and the COPR blade sets are the collective pitch settings. The Opt-III was optimized using both hover and forward flight conditions, whereas the COPR-3 was only optimized using the forward flight condition. The resulting twist distribution of the COPR blade, therefore, tends to be quite aggressive when considering a hovering mode of flight. As a result, the COPR blades required a collective

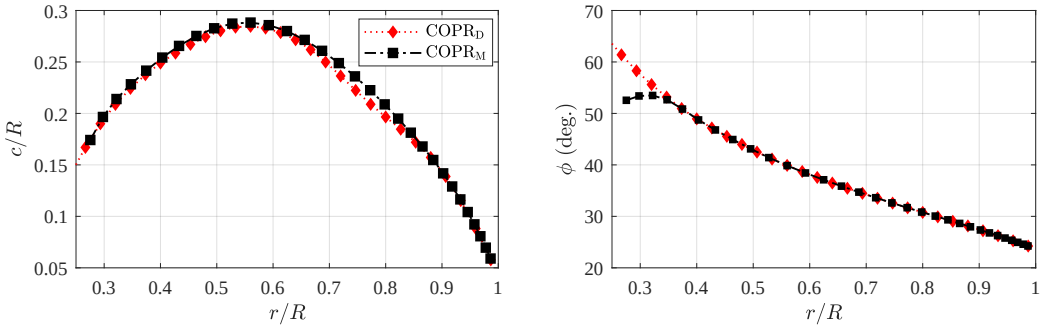

(a) Chord distributions

(b) Twist angle distributions

Figure 6. Comparison of blade (a) chord distributions and (b) twist angle distributions between the COPR nominal blade design and manufactured shape.

adjustment to yield suitable hover performance, whereas the Opt-III maintained a constant collective for both modes of flight. Specifically, **the COPR blades were set to a $-15°$ collective reduction for hovering modes of flight** relative to the design twist distribution provided in Fig. 6(b). A description of how the blade collectives were mechanically measured during testing is provided in Section 3.2.

3 Experimental Technical Approach

3.1 Testing Facility and Instrumentation

Tests were conducted in the NASA Langley Low Speed Aeroacoustic Wind Tunnel (LSAWT). The LSAWT is an open-circuit free-jet wind tunnel that is currently configured for a freestream Mach number range of $0.045 \leq M_\infty \leq 0.143$ and is reconfigurable to an upper end capability of $M_{\infty,\max} = 0.32$. As shown in Fig. 7(a), the test section is centrally located along the length of the facility, and it is acoustically treated down to an approximate cut-on frequency of 250 Hz. More details of the facility capabilities can be found in Ref. [16]. A streamwise linear array of 28 Brüel & Kjær type 4939 free-field microphones was used to provide acoustic spectra and directivity information across a wide range of observer angles. Specifically, the array spans a geometric observer angle range of $40° \leq \theta_o \leq 147.5°$. As is shown in Figs. 7(b) and 7(c), the linear microphone array is located along one of the facility upper corners in the streamwise direction at an inclination angle of $\Psi_o = 50°$ and a distance of 3.54 m from the tunnel (and test article) centerline. This distance represents the closest microphone location to the proprotor test articles, which corresponds to a minimum distance of 11.6 proprotor radii. This provides assurance that the microphones in the array are in the acoustic far field of the proprotor source.

3.2 The Propeller Test Stand

The NASA Langley Propeller Test Stand (PTS) was designed for the aerodynamic and acoustic evaluation of propeller/rotor systems across multiple NASA wind tunnel facilities. It contains a water-cooled drive motor that is capable of continuous

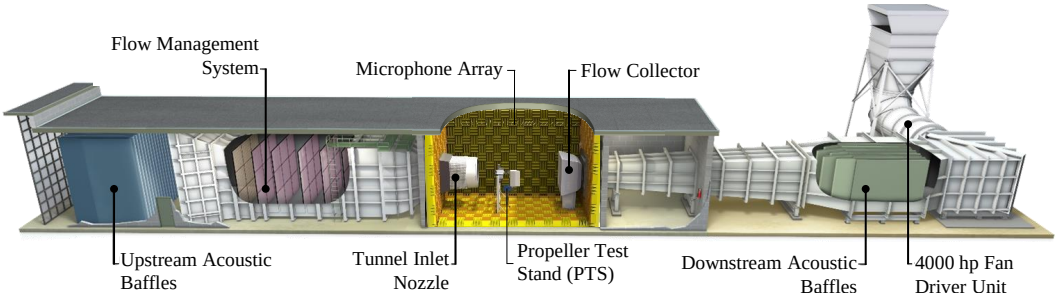

(a) Facility cut-away rendering

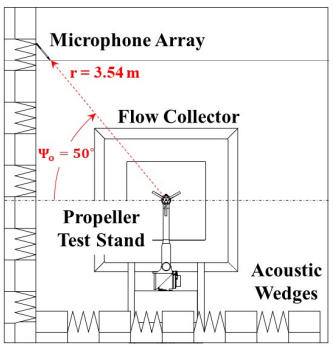

(b) Downstream view

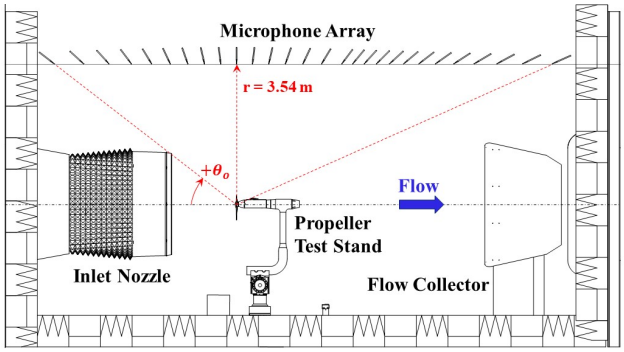

(c) Sideline view

Figure 7. Primary components of the LSAWT facility and test section schematics.

52 kW, 15,000 RPM operation with an operational speed range of 250 to 16,000 RPM. The PTS has a rotation rate accuracy of ± 1 RPM, which is controlled by a dedicated variable frequency drive. It has roll, pitch, and yaw capabilities with respective angular ranges of ±180°, ±25° for nonzero-yaw conditions, and ±90°, all to an accuracy of ±0.1°. For zero-yaw conditions, the PTS is capable of an increased pitch angle range of -25° (forward tilt) to +90° (rearward tilt). The PTS also has onboard instrumentation including an ATI-IA Mini85 six-component multiaxis load cell for aerodynamic load measurements, a rear-mounted triaxial accelerometer for vibration assessments, a laser sensor tachometer for tracking motor revolutions, and four onboard temperature probes to monitor motor and bearing health. Figure 8 provides a photograph of the PTS installed in the LSAWT with annotations of the stand's rotational degrees of freedom.

The collective settings of the blades on the PTS were measured mechanically using a set of inclinometers. The collectives of the C24ND and Opt-III blades were assessed by measuring the geometric angle of the airfoil profile at the blade tip using a commercial off-the-shelf propeller pitch gauge, while the COPR blade pitch was measured using a calibrated inclinometer that was positioned on a customized 3D printed pitch block that matched the top surface contour of the blade at a midspan location along the blade. Figure 9 provides images of the COPR blade pitch measurement setup hardware. These different measurement methods between the two blade sets were required due to the vastly different blade shapes, particularly in terms of the dramatic chord taper present on the COPR blades. The output of the

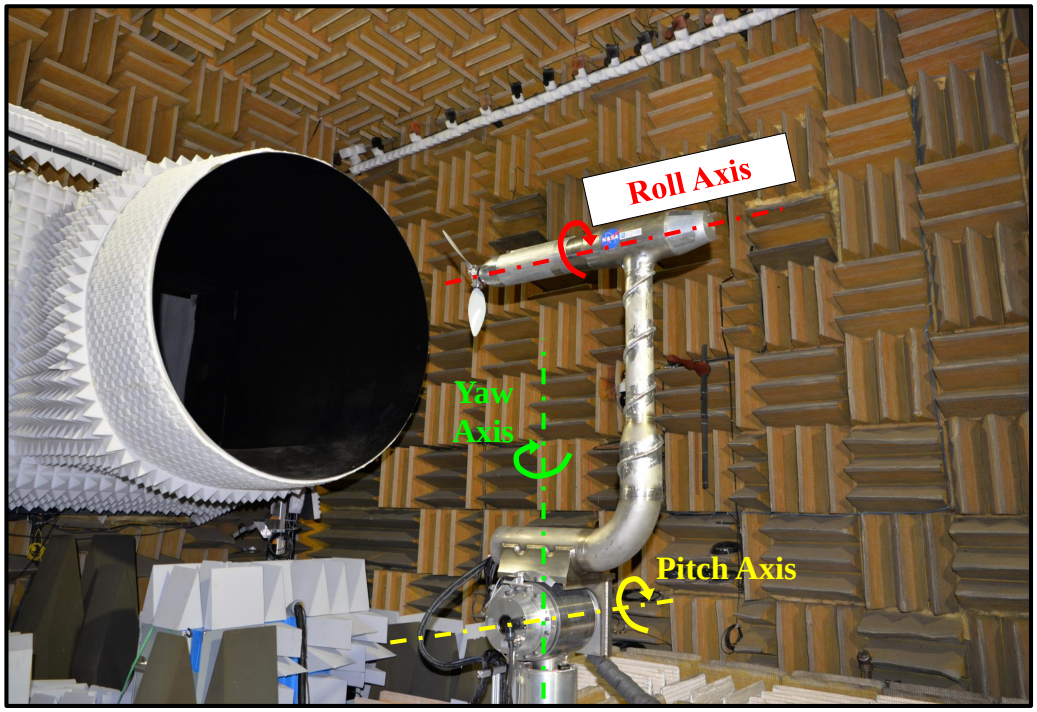

Figure 8. Image of the PTS installed in the LSAWT with annotated rotational degrees of freedom. *Note: COPR-3 proprotor installed.* [Source: NASA]

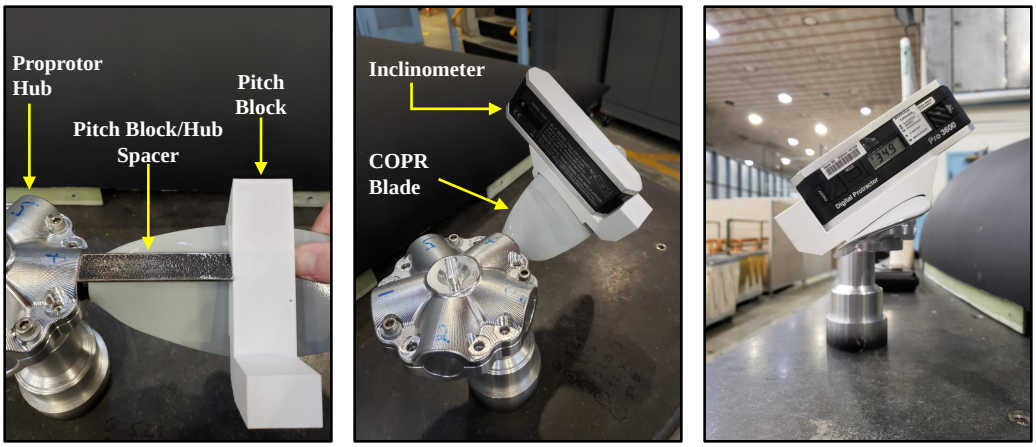

(a) (b) (c)

Figure 9. Images of hardware used to set pitch (collective) on the COPR blade: (a) top-down view illustrating pitch block placement on a blade, (b) isometric view showing digital inclinometer placement, and (c) image looking from blade tip to root for angle measurement. [Source: NASA]

commercial propeller pitch gauge was validated against the calibrated inclinometer to ensure the relative accuracy between the two measurement methods.

3.3 Data Acquisition and Processing

3.3.1 Hardware and Acquisition Settings

Dynamic data were acquired on National Instruments dynamic signal acquisition modules installed in a PXIe-1085 chassis. Microphone data were acquired on several PXIe 4480 modules at a sampling rate of 204.8 kSamples/s, while load cell data were acquired on a single PXI 6143 module at a lower sampling rate of 80 kSamples/s. Microphone and vehicle performance data acquisitions were divided between these two module types to allow for real-time monitoring of the performance data. Microphone data were high-pass filtered at 10 Hz, which provided a usable flat passband (less than -0.5 dB deviation) within a frequency range of 50 Hz $\leq f \leq$ 80 kHz. Load cell data were low-pass filtered at 32 kHz and DC-coupled to allow for steady load measurements. Filter and channel gain settings were implemented by running the microphone and load cell channels through a Precision Filter 28000 series chassis. Each wind tunnel run was acquired for a time duration of 20 seconds.

3.3.2 Periodic and Broadband Noise Extraction

Acoustic data were processed using three different techniques [17–19]. The first and simplest of these is the narrowband spectrum (method **1**), which is computed using the Fast Fourier Transform with a Hanning window with 75% overlap and a frequency resolution of 10 Hz. This yields a normalized autospectral random uncertainty of $\epsilon_r = 5.68\%$ [20], which translates to a dB uncertainty of ± 0.25 dB.

The second processing technique allows for the separation of periodic and random noise components in the time domain (method **2**). The transistor-transistor logic pulse signal from the tachometer was used to parse the time series data into blocks corresponding to individual revolutions of the rotor. This allowed for the calculation of a mean rotor revolution time history, which was then repeated, then subtracted from the original time record. This provides both nominally *periodic* and *residual* time histories, which can then be converted into the frequency domain using the first processing method.

The third method is similar to the previous one in that it uses the tachometer signal to parse the acoustic data time histories into individual rotor revolutions. It involves narrow band-pass filtering of the acoustic time series to retain only harmonics of the rotor blade passage frequency (BPF) (method **3**). The purpose of this method is to more accurately compare acoustic amplitudes at principal frequencies of interest – namely harmonics of the BPF – between predictions and experiment. For the current study, the majority of the presented data is limited to the first three harmonics of the BPF. To isolate the acoustic contributions at these specific frequencies, 2nd-order Butterworth narrow band-pass filters were applied to the time series data, with a $\pm$ 20 Hz frequency band centered around the frequency of interest. Acoustic amplitudes of each frequency of interest were computed by calculating the RMS of the ensemble-averaged filtered pressure time history across all revolutions:

$$SPL_{\mathrm{n*BPF}} = 20\log_{10}\left(\frac{\bar{p}_{rms}}{p_{ref}}\right). \tag{3}$$

Furthermore, the uncertainties of these tonal amplitudes were approximated by the standard deviations (σ) of the RMS pressure values:

$$u_{SPL_{\mathrm{n*BPF}}} = 20\log_{10}\left(\frac{\bar{p}_{rms} \pm \sigma_{p_{rms}}}{p_{ref}}\right). \tag{4}$$

It is important to note that some extracted tonal harmonics were computed to be less than the raw spectral level calculated using the first processing method, which tends to correspond to rather large standard deviations, and thus relatively high uncertainty values. Due to the presentation of these tonal harmonics on a dB scale, the lower bounds of these uncertainties can become complex-valued. This is a limitation of the approximation used, and could be avoided with a more robust uncertainty analysis. Therefore, the uncertainty bounds for these tonal harmonics will be presented using the upper limit as a symmetric uncertainty bound quantity:

$$u_{SPL_{\mathrm{n*BPF}}} = \pm 20\log_{10}\left(1 + \frac{\sigma_{p_{rms}}}{\bar{p}_{rms}}\right). \tag{5}$$

Figure 10 provides a summary of the three different acoustic post-processing methods used in this study, applied to the forward flight (cruise) flight condition of all four tested proprotors at a corrected in-plane microphone measurement ($\theta_c = 90°$). This microphone location correction process is discussed in Section 3.3.3. More information on this microphone correction method is provided in the next section. As the figure shows, the three processing techniques are effective at dividing the raw autospectra into their periodic and broadband counterparts. However, the results of method 2 for the C24ND and Opt-III do show residual tonal peaks in the broadband spectra, the cause of which is currently unknown. It is also worth noting that some of the extracted BPF harmonics (method 3) for the COPR-3 and COPR-5 proprotors appear at or even below the baseline spectral "shelf" (method 1). This greatly increases the measurement uncertainty of the tonal amplitude, which was discussed previously. Figure 11 shows the post-processing techniques applied to the in-plane microphone measurements of the proprotors in the target hovering condition. While these processing techniques yield similar results as the forward flight cases, there is considerably more apparent tonal content retained in the residual broadband spectra. This is believed to be due to the ingestion of turbulent gusts into the proprotor disks through the wind tunnel inlet nozzle, which result in excited harmonics that are of random phase. Overall this is believed to be due to the fact that the proprotors tested in this study have disk areas that are approximately 32% of the LSAWT inlet nozzle area. As a result, operating the proprotors at high thrust pulls in the outside air, which also produces a shear layer with the inside ambient air of the LSAWT test cell. The resulting excitation of the BPF harmonics resembles that which occurs as a result of operation of a propeller or rotor in a closed environment, namely due to flow recirculation [21].

Finally, two acoustic metrics are used in this study for both comparisons between flight conditions and between periodic and broadband noise contributions. They are the sound pressure level (SPL) spectrum, and the overall sound pressure level (OASPL) denoted by L. All tonal (periodic) OASPLs are calculated over

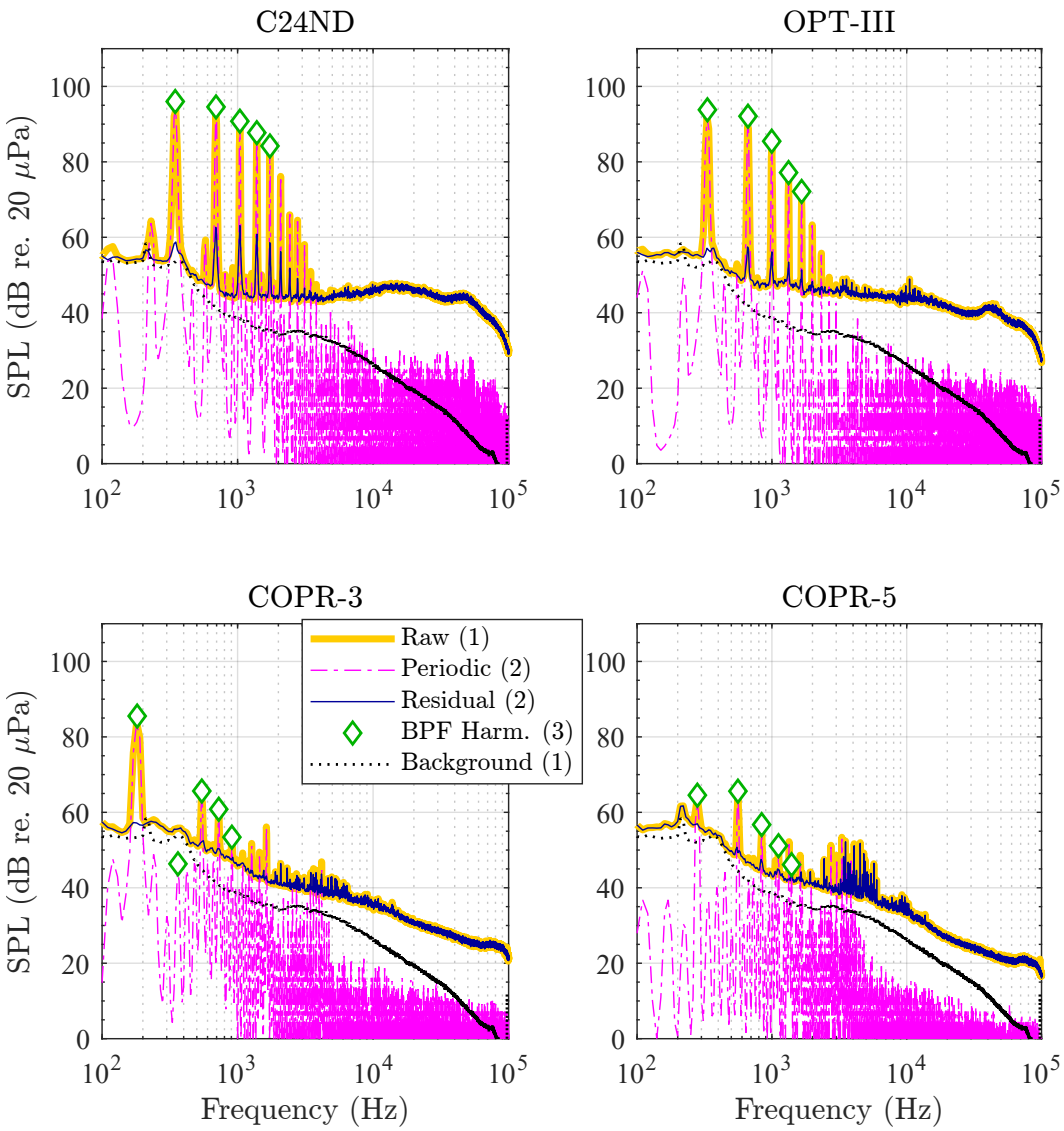

Figure 10. Narrowband acoustic spectra of the tested proprotors at design forward flight (cruise) condition at $\theta_c = 90°$ illustrating acoustic post-processing methods. *Note: tunnel background noise (no propeller in operation) at $M_\infty = 0.111$; methods indicated in parentheses; first five extracted BPF harmonics using method 3 are shown.*

a frequency range of $100 \leq f \leq 80,000$ Hz, whereas broadband (residual) OASPLs are computed over $1,000 \leq f \leq 80,000$ Hz for forward flight conditions and $100 \leq f \leq 80,000$ Hz for hover conditions. The truncated frequency range of integration for broadband OASPL in forward flight is due to facility background noise contamination at frequencies below 1,000 Hz for the flow conditions shown in this document. Furthermore, broadband OASPLs in forward flight are computed after subtracting the facility background noise levels. It will be shown that this background subtraction only impacted the broadband OASPL calculations of the

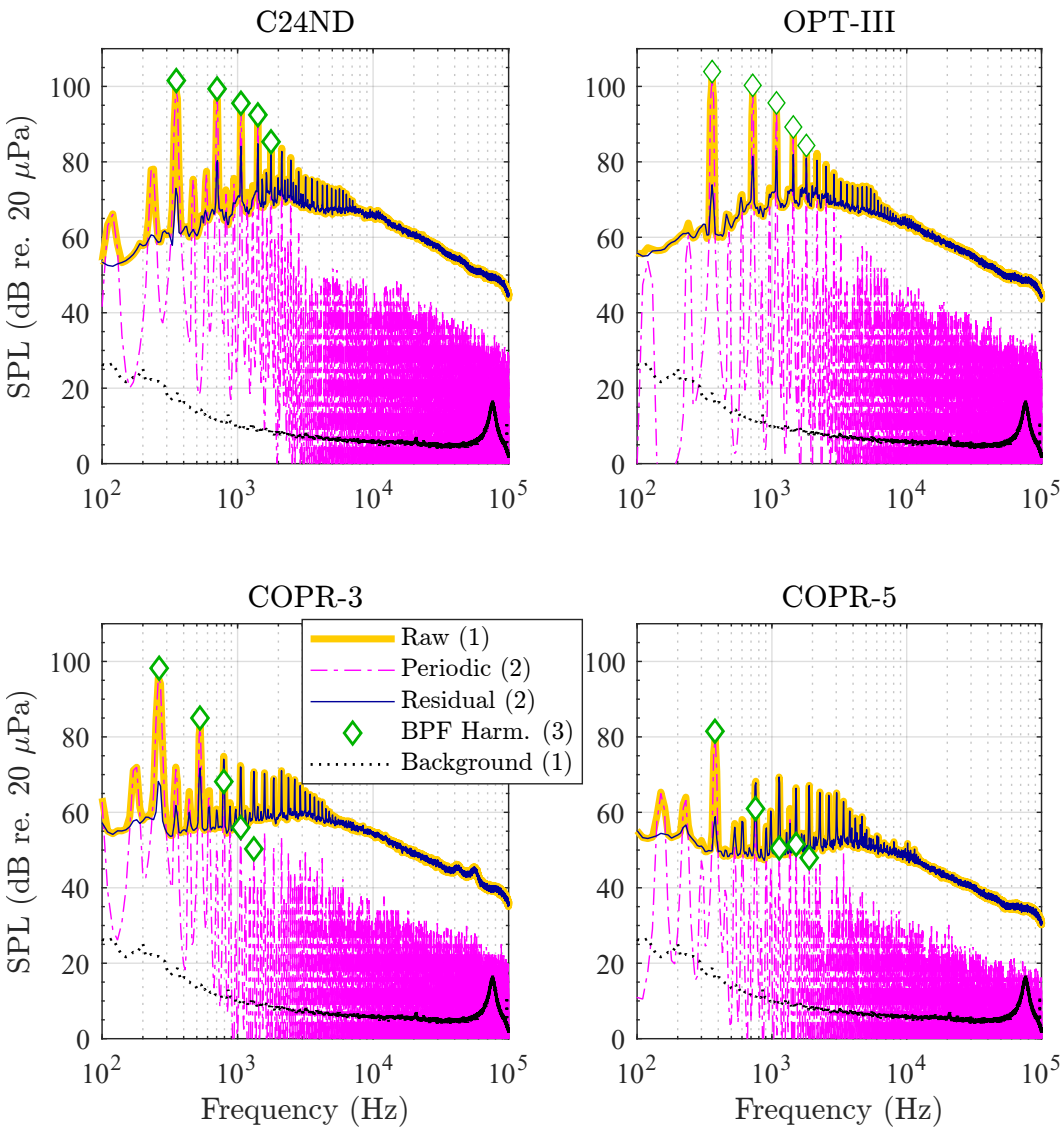

Figure 11. Narrowband acoustic spectra of the tested proprotors at design hover condition at $\theta_o = 90°$ illustrating acoustic post-processing methods. *Note: tunnel background noise (no propeller in operation) at static conditions; methods indicated in parentheses; first five extracted BPF harmonics using method 3 are shown.*

COPR-3 and COPR-5 proprotors, due to their relatively low broadband noise content.

3.3.3 Shear Layer and Atmospheric Absorption Corrections

Flow through the open test section of the LSAWT results in the formation of a shear layer between the open jet core flow and the ambient test cell chamber [16, 22]. As a result, sound waves that are generated by a source located in the core flow are refracted and potentially scattered as they pass through this shear layer.

Therefore, corrections are applied to the measured data to account for the effective corrected microphone position. These include a corrected microphone radial location r_c, radiation angle θ_c, and a dB level correction ΔdB_c. These corrections are made with the intent of representing the microphone measurement as an observer **moving with the source**. This is nominally equivalent to a microphone measurement in a closed wind tunnel (flow over both source and observer). Included in the shear layer level correction is a spherical spreading correction applied to the measured data to correct the observer distance back to one on the original line of observers in the LSAWT microphone array. In other words,

$$SPL_c = SPL_m + \Delta\text{dB}_c + \Delta\text{dB}_{r_c/r_{LSAWT}}, \tag{6}$$

where SPL_m is the raw SPL measured by the microphone and $\Delta\text{dB}_{r_c/r_{LSAWT}}$ is the distance correction equivalent to

$$\Delta\text{dB}_{r_c/r_{LSAWT}} = 20\log_{10}\left(\frac{r_c \sin\theta_c}{3.54}\right), \tag{7}$$

where $r = 3.54$ m is the constant orthogonal distance between the LSAWT microphone array line of observers and the LSAWT tunnel centerline, which also corresponds to the proprotor axis of rotation. Appendix A provides the geometric and corrected LSAWT microphone locations as well as the amplitude corrections applied using the methods of Ref. [22].

Atmospheric attenuation is computed using ANSI S1.26-1995 and is a function of facility ambient pressure, temperature, relative humidity, and frequency. It is effectively "removed" from the LSAWT microphone data using the shear layer-corrected microphone location relative to the proprotor as the effective source-to-receiver distance. The resulting spectrum is assumed to be "lossless." Figure 12 presents a visual illustration of the effect of removing the atmospheric attenuation from the raw LSAWT data for two microphones at considerably different distances from the proprotor source. The impact to the measured spectrum is seen to only become visible at frequencies above 30 kHz for the microphone located at $\theta_c = 90°$, whereas it can be seen to present itself starting around 20 kHz for $\theta_c = 155°$. This is due to the fact that this microphone is much further away from the source region than the one at $\theta_c = 90°$. It is important to note that neither shear layer nor atmospheric attenuation amplitude corrections are applied to time series data presented in this document.

3.3.4 Thermal Drift Considerations with Load Cell Data

The load cell utilized in this study was prone to thermal drift effects, particularly for long duration testing sequences. Thermal drift could occur as a result of varying facility ambient temperatures as well as local temperature gradients seen by the load cell caused by the PTS motor itself. This could result in potentially inaccurate thrust and torque measurements. The thrust measurement, in particular, was found to be most sensitive to these thermal drift effects. This is due to the fact that dimensional thrust measurement was heavily reliant on the voltages output by all

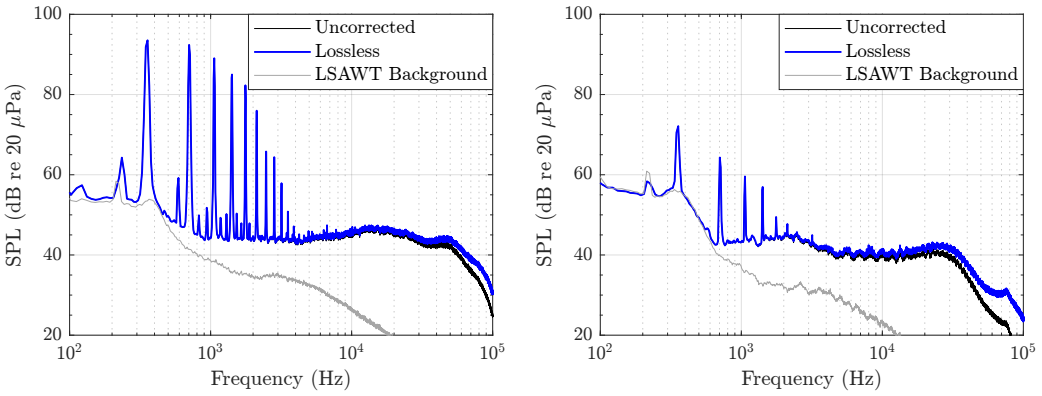

(a) $\theta_c = 90°$ (b) $\theta_c = 155°$

Figure 12. Removal of atmospheric attenuation from raw acoustic spectra measured (a) in the plane of the proprotor and (b) furthest downstream of the plane of the proprotor. Data correspond to the C24ND baseline propeller operating in forward flight. *Note: no shear layer correction applied.*

strain gages in the load cell. Therefore, if any combination of these strain gages were to exhibit even small amounts of drift, they would potentially accumulate and present a considerable steady-state drift on the thrust load measurement.

To reduce the effects of thermal drift on the load cell measurements, a "thermal soaking" procedure was implemented. This process consisted of operating the PTS with proprotor installed at the maximum tested rotation rate for that specific proprotor for a period of time. This was done in an attempt to establish a thermal equilibrium between the LSAWT inlet and the test section chamber to better ensure a more stable thermal environment. For hover measurement sets, the PTS was operated with no tunnel flow, whereas the LSAWT was operated at a freestream condition of $M_\infty = 0.111$ for forward flight data sets during the thermal soaking. This freestream condition was selected since it represented an approximate middle range of the speeds tested in this campaign. The PTS would then be shut off and a zero load, or "tare" condition would be taken, after which a testing sequence (either hover or forward flight) would continue. The time durations of these thermal soaking runs varied anywhere between five and fifteen minutes, depending on temperature conditions of the day.

Thermal drift was assessed by means of comparing zero load, or tare runs, both prior and after a set of test runs. The level of difference between the zero load values of the load cell for these two "wind-off" conditions was approximated as the level of load measurement uncertainty (or repeatiblity error) for that set of data. To simplify the post-processing of the data spanning the range of tested proprotors and flight conditions, a single "worst-case" measured uncertainty was used for the different sets of flight conditions. In other words, the largest measured uncertainties for a set of hover runs were used for the entirety of the acquired hover data, and likewise for the forward flight data sets. The repeatability errors used for the performance data presented in Section 4 are provided in Table 3. These uncertainties are presented in the form of error bars in the following section.

Table 3. Thrust and torque repeatability errors for hover and forward flight conditions.

Flight Condition	Thrust (N, lbs.)	Torque (N-m, lbf-in.)
Hover	6.67, 1.50	0.17, 1.50
Forward Flight	8.90, 2.00	0.17, 1.50

4 Aerodynamic Performance Trends

This study investigates flight conditions conventionally corresponding the operation of both a rotor (hover or VTOL mode) and a propeller (axial forward flight). Aerodynamic performance coefficients are classically defined differently for rotors and propellers. Therefore, both types of performance definitions will be discussed in the following sections.

4.1 Axial Forward Flight Performance

The forward flight aerodynamic performances of the tested proprotors are defined in this section using conventional propeller nomenclature. Thrust, power, and propulsive efficiency coefficients are defined as

$$C_{T,F} = \frac{T}{\rho_\infty n^2 D_p^4}, \tag{8}$$

$$C_{P,F} = \frac{P}{\rho_\infty n^3 D_p^5}, \tag{9}$$

and

$$\eta = \frac{C_{T,F} J}{C_{P,F}} = \frac{T U_\infty}{P}, \tag{10}$$

where T is the rotor thrust perpendicular to the hub plane, P is the rotor power, ρ_∞ is the ambient air density, D_p is the proprotor diameter, n is the rotation rate of the proprotor in revolutions per second, and J is the forward flight advance ratio. The dimensional power P of the system is further defined as

$$P = Q\Omega, \tag{11}$$

where Q is the rotor torque in the hub plane and Ω is the rotor rotational speed in rad/s. The advance ratio, J is further defined as

$$J = \frac{U_\infty}{n D_p} = \frac{M_\infty \pi}{M_{\text{tip}}}, \tag{12}$$

where the proprotor tip Mach number is computed as

$$M_{\text{tip}} = \frac{\Omega R}{c_\infty}, \tag{13}$$

where $R = D_p/2$ is the proprotor tip radius and c_∞ is the ambient speed of sound in the testing facility. Dimensional thrust and power are presented in the form of

a *sea level at standard day* (SLSD) equivalency, which is denoted by $[\ ]^*$, and are defined by

$$T^* = T \times \frac{\rho_{SLSD} c_{SLSD}^2}{\rho_\infty c_\infty^2} \tag{14}$$

and

$$P^* = P \times \frac{\rho_{SLSD} c_{SLSD}^3}{\rho_\infty c_\infty^3}. \tag{15}$$

Figures 13 - 16 provide the dimensional and nondimensional performance characteristics of the tested proprotors as a function of forward flight advance ratio, J. The range of advance ratio conditions in these figures correspond to wind tunnel speeds between $0.048 \leq M_\infty \leq 0.143$. The C24ND data in Fig. 13 are for a single tip speed condition of $M_{\text{tip}} = 0.66$. Both the dimensional and nondimensional thrust and power profiles reveal an expected reduction in these quantities with increasing advance ratio, or in this case, tunnel speed. The efficiency profile in Fig. 13(e) reveals a peak efficiency in the vicinity of $J = 0.525$, which corresponds to the target forward flight thrust condition of $T^* = 106.5$ N (24 lbs.), which can be seen in Fig. 13(a). It is worth noting that while the uncertainties (i.e., error bars) for Figs. 13(a) - 13(d) are modest relative to the mean data values, those for the propulsive efficiency data in Fig. 13(e) can become quite large, particularly at high advance ratios. This is due to the coupling of the uncertainties associated with the individual thrust and torque (power) quantities via Eq. 10.

The Opt-III was tested in forward flight at four different tip speed conditions. Figure 14 shows how well the dimensional thrust and power data collapse as a result of the nondimensionalization of these data to $C_{T,F}$ and $C_{P,F}$. It is also worth noting that the data shown in these plots contain a number of repeat test points at the two lower tested M_{tip} conditions. This was done in an effort to determine the stability and repeatability of the load measurements for nominally identical operating conditions at different times during the testing sequence. These repeat data points show remarkably good agreement with the original test points, ensuring a reliable data set.

Figure 15 provides the dimensional and nondimensional performance data for the COPR-3 proprotor in forward flight at three different tip Mach number conditions. Nondimensionalization of the loading data are again seen to provide an effective data collapse, especially for the $C_{P,F}$ profile data. If attention is focused on Fig. 15(e), however, it can be seen that a set of repeat points for $M_{\text{tip}} = 0.25$ and $J \approx 1.14$ show a considerably larger deviation in propulsive efficiency than previously shown for the Opt-III data. This is again due to thermal drift of the load cell for this set of data. However, it should also be noted that the differences in these data points are rather small compared to the error bars that encompass them. This can also be explained by the rather long time period between the last wind tunnel test point and the post-run tare measurement, over which additional load cell thermal drift could accumulate. This could suggest that this repeatability assessment method requires improvement for future tests.

Figure 16 provides the performance data for the COPR-5 proprotor at two tip Mach number conditions. Data are again seen to collapse very well in Figs. 16(c)

– 16(e). Note that only two tip Mach number conditions were run as a result of tunnel test time limitations. Repeat test points are presented at $J \approx 0.6$ and $J \approx 1.1$ for $M_{\text{tip}} = 0.25$ and $M_{\text{tip}} = 0.32$, respectively. These repeat points are difficult to discern from the original points in the test sequence, which indicates excellent measurement repeatability for this set of data.

Finally, Fig. 17 provides a summary of the propulsive efficiencies for the tested proprotors, each for a constant tip Mach number condition. As Fig. 17(a) shows, the C24ND and Opt-III proprotors have overall similar efficiency profiles over a very similar advance ratio range. The most noticeable difference between these proprotors is that the Opt-III is seen to outperform the C24ND at higher advance ratios, while it underperforms at lower advance ratios. Furthermore, the COPR-3 and COPR-5 proprotors are seen to operate over a much different advance ratio range than the C24ND and Opt-III. This is due to the considerably lower tip speeds at which these proprotors are designed to operate. A more consolidated way to view these curves is presented in Fig. 17(b), which shows the proprotor efficiency profiles as a function of freestream Mach number. As this figure shows, the C24ND, Opt-III, and COPR-3 proprotors all perform at nearly an identical peak propulsive efficiency for the target forward flight condition at $M_\infty = 0.111$. There is a noticeable degradation in performance for the COPR-5 proprotor, which is expected since it represents an off-design proprotor configuration. In other words, it is simply the result of increasing the blade count of a proprotor designed as three-bladed (the COPR-3). Therefore, it is expected that its performance would deviate from that of the original target design.

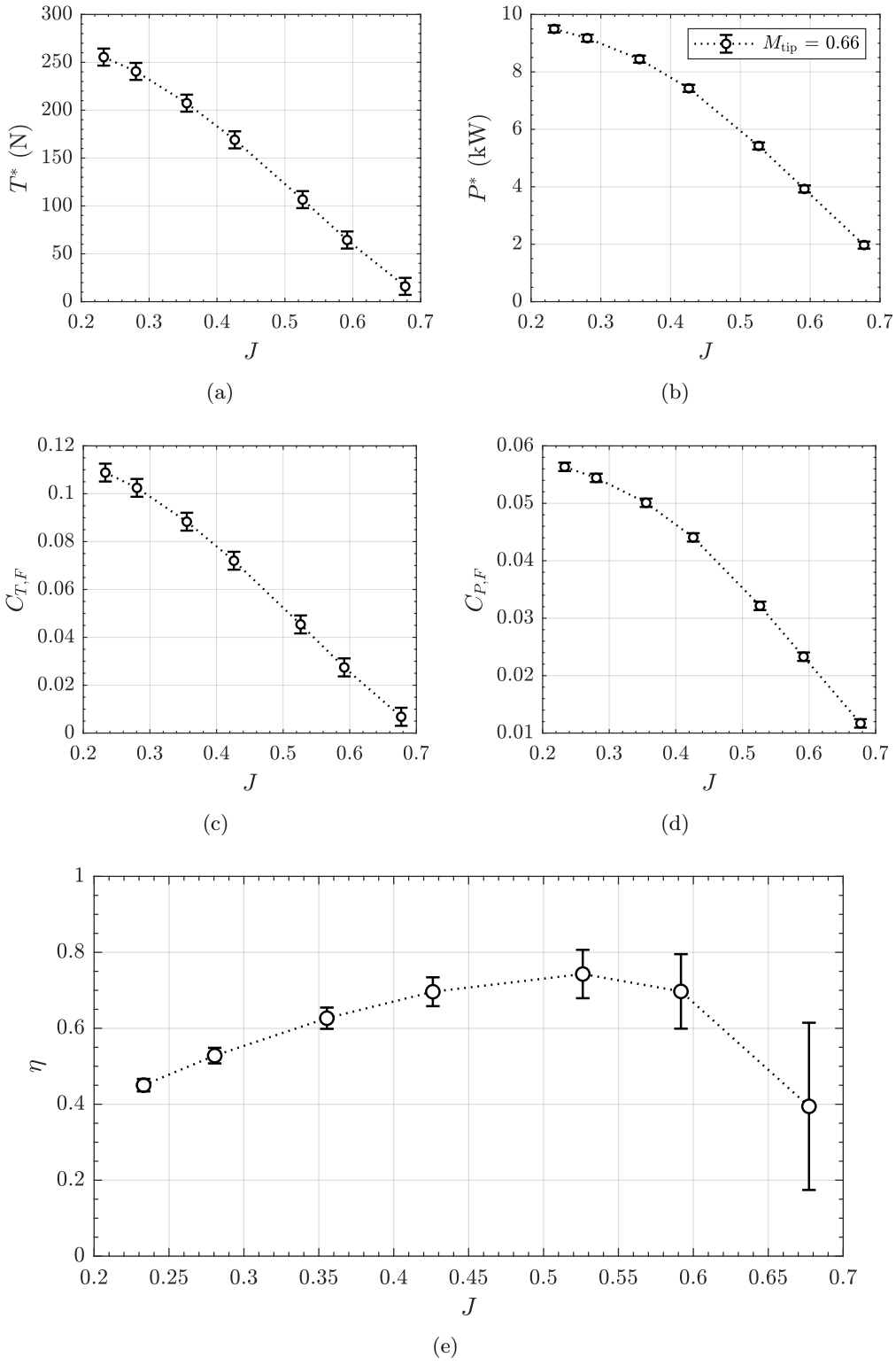

Figure 13. Thrust, power, and propulsive efficiency profiles for the C24ND propeller for the range of tested advance ratios at $M_{tip} = 0.66$.

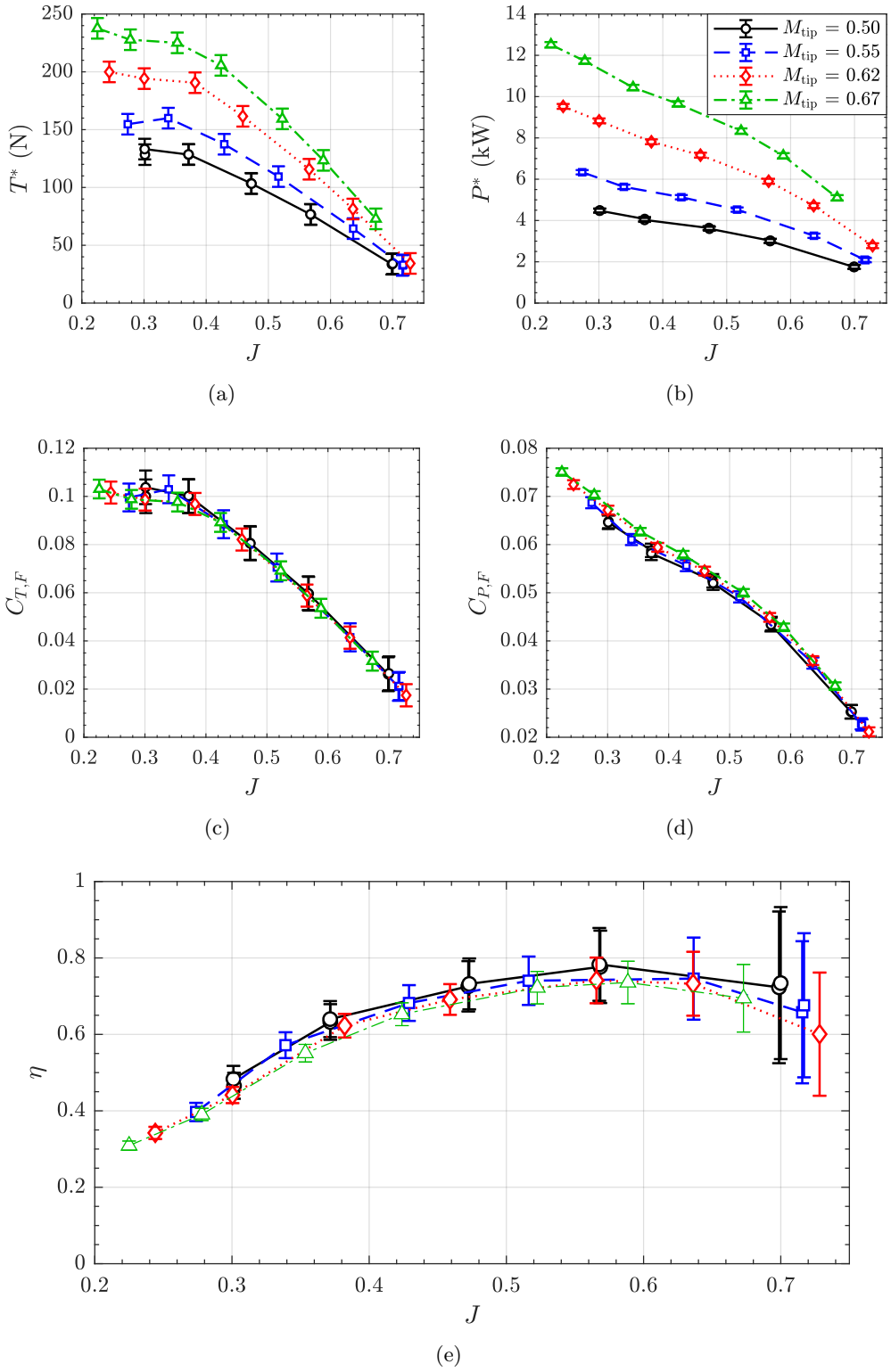

Figure 14. Thrust, power, and propulsive efficiency profiles for the Opt-III proprotor for the range of tested advance ratios at four different tip Mach numbers.

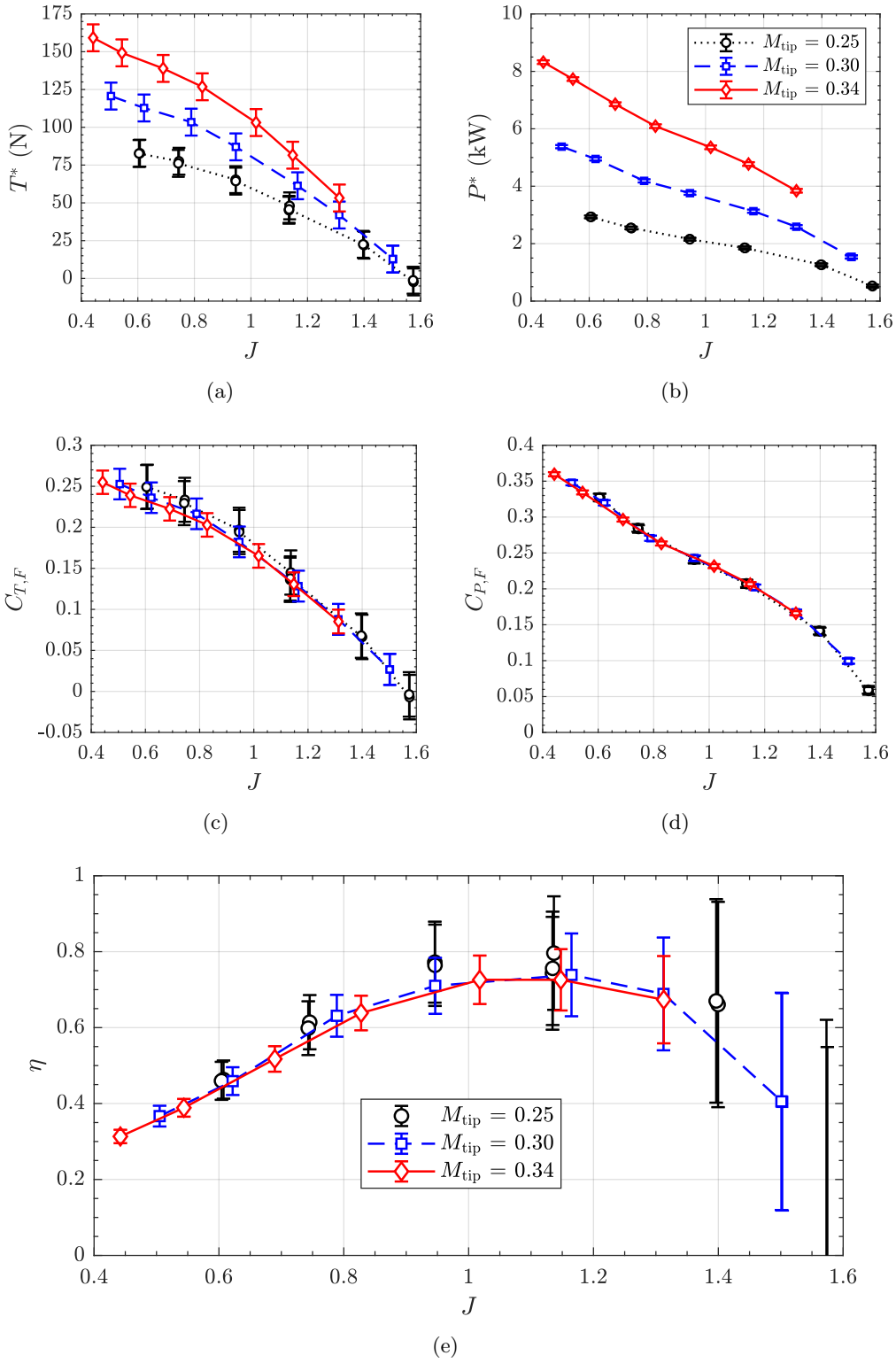

Figure 15. Thrust, power, and propulsive efficiency profiles for the COPR-3 propro-tor for the range of tested advance ratios at three different tip Mach numbers.

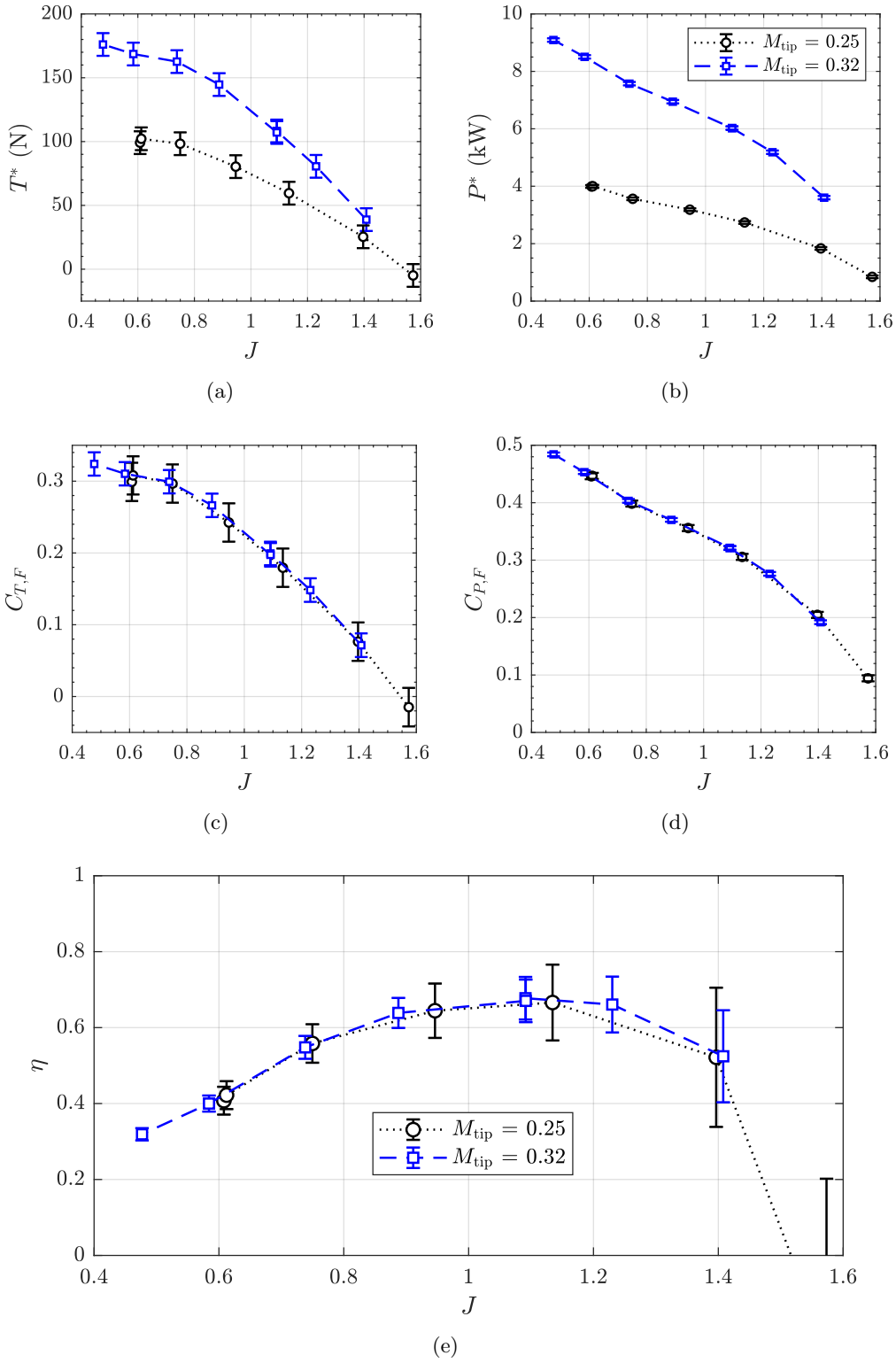

Figure 16. Thrust, power, and propulsive efficiency profiles for the COPR-5 propro-tor for the range of tested advance ratios at two different tip Mach numbers.

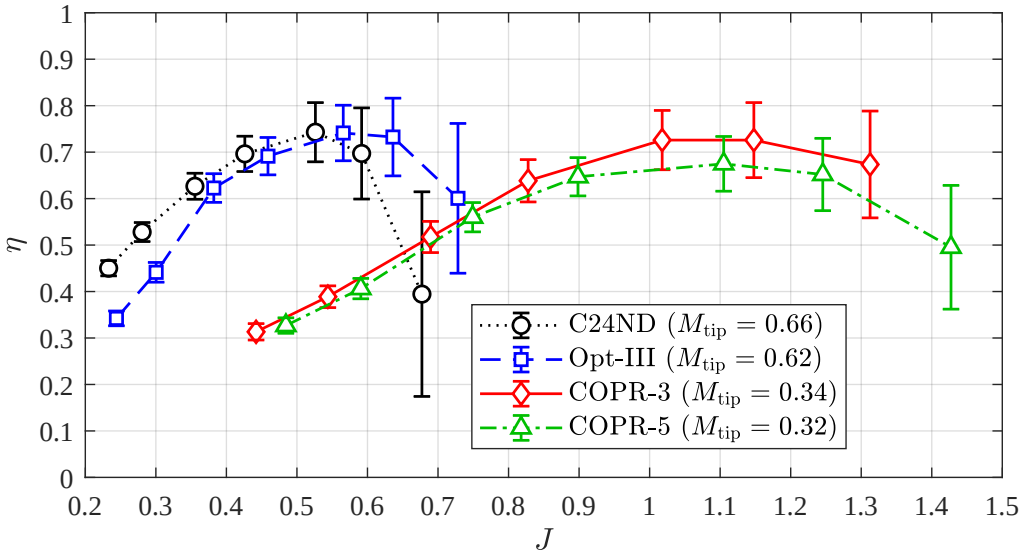

(a)

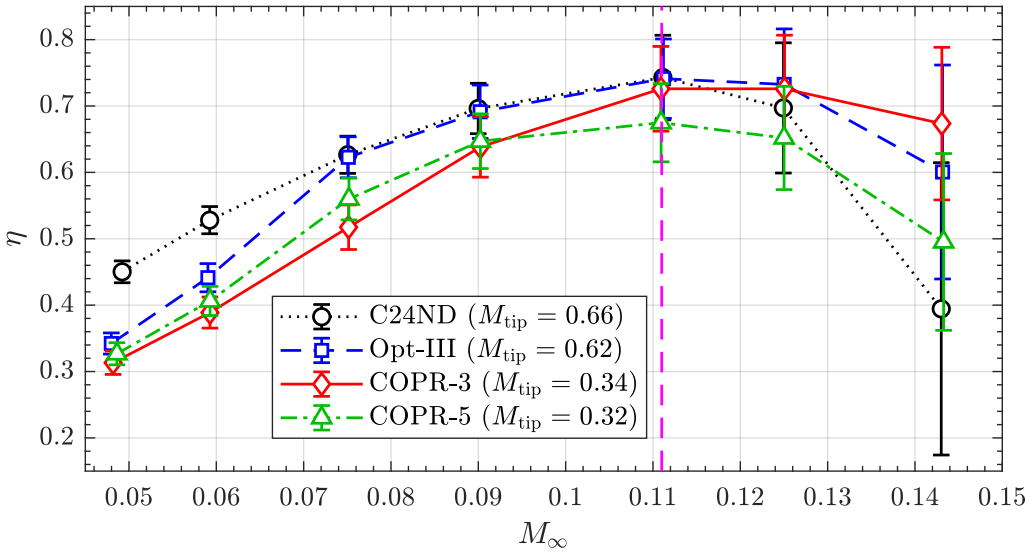

(b)

Figure 17. Propulsive efficiencies for the tested proprotors plotted against (a) propeller advance ratio and (b) freestream Mach number. *Note: target cruise condition denoted by '- - -' in (b).*

4.2 Hover Performance

The hover performances of the proprotors tested in this study are analyzed using conventional rotor terminology: the hover thrust coefficient ($C_{T,H}$), power coefficient ($C_{P,H}$), and figure of merit (FM). These are defined as

$$C_{T,H} = \frac{T}{\rho_\infty A \Omega^2 R^2}, \tag{16}$$

$$C_{P,H} = \frac{P}{\rho_\infty A \Omega^3 R^3}, \tag{17}$$

and

$$FM = \frac{T^{\frac{3}{2}}}{Q\Omega\sqrt{2\rho_\infty \pi R^2}} = \frac{C_{T,H}^{3/2}}{\sqrt{2}C_{P,H}}, \tag{18}$$

where $A = \pi R^2$ is the rotor disk area. All other pertinent quantities are defined in Section 4.1.

Figure 18 shows the dimensional thrust, power, and associated thrust and power coefficients as a function of proprotor tip Mach number in static hover conditions. The data in Figs. 18(a) and 18(b) show performance trends following a quadratic profile with tip Mach number. Figures 18(c) and 18(d) show the resulting nondimensional force coefficient profiles. As Figs. 18(a) and 18(c) show, the thrust behaviors between the C24ND and Opt-III are very similar. The power profiles in Figs. 18(b) and 18(d), however, show considerably different power profiles.

Figure 19 shows the figures of merit of the proprotors plotted against tip Mach number, as well as a nondimensional thrust setting, $C_T M_{\text{tip}}^2$. This nondimensional term effectively alters the thrust coefficient as

$$C_T M_{\text{tip}}^2 = \frac{T}{A\rho_\infty c_\infty^2}. \tag{19}$$

This nondimensionalization effectively removes the dependence on tip Mach number, and changes it to a thrust condition normalized by $\rho_\infty c_\infty^2$. It is important to note that interpretation of the data in Fig. 19 must be done with care. Due to the wide range of rotor solidities between these proprotors, direct comparisons are not necessarily appropriate. However, some interesting observations can still be made. In particular, the Opt-III proprotor is seen to exhibit lower overall FM for all tested tip speeds relative to the C24ND. This can be related back to the nearly identical thrust profiles between these two proprotors, yet considerably higher power draw profile for the Opt-III proprotor shown previously in Fig. 18.

Figure 20(a) provides a comparison of dimensional power versus thrust between the different proprotors. This provides a method of comparing aerodynamic performance characteristics that is similar to a figure of merit, but in terms of dimensional load conditions. Figure 20(b) also provides the power loading (thrust per unit power) of the proprotors as a function of disk loading (thrust per unit area). This type of performance metric is useful because it represents an absolute measure of efficiency without any underlying assumptions. It also allows for a better way to

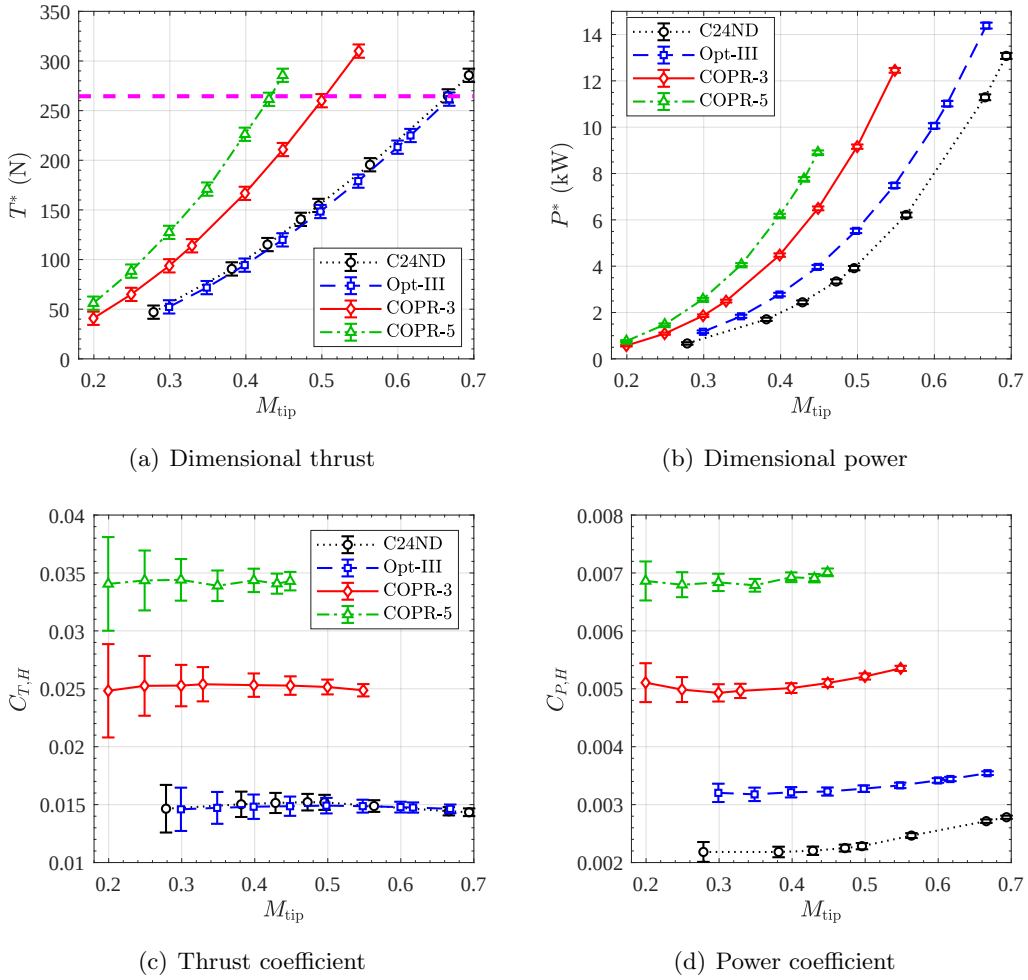

(a) Dimensional thrust

(b) Dimensional power

(c) Thrust coefficient

(d) Power coefficient

Figure 18. Hover thrust and power variations with tip Mach number for the tested proprotors. *Note: target hover thrust condition denoted by '- - -' in (a).*

compare performance behaviors between proprotors of different diameters, namely the Opt-III as compared to the other tested proprotors. The power loading data of Fig. 20(b) are accompanied by third-order polynomial curve fits to the discrete run data points to allow for interpolation of the trends to a common disk loading condition. As Fig. 20 shows, the Opt-III proprotor is seen to perform worse than the baseline C24ND, evidenced by the higher required power draw at the target thrust condition relative to the C24ND. Specifically, the Opt-III has a power loading that is 22% higher than that of the C24ND at the common indicated disk loading condition. This is in contrast to the COPR-3 and COPR-5 proprotors, which indicate power loading reductions at this disk loading condition of 22% and 43%, respectively. It is again worth reiterating that these power loading comparisons are based on the interpolated data points corresponding to the target disk loading condition of the C24ND. It is also worth noting that these comparisons are very similar to the case as if they were computed using the indicated discrete measured data points.

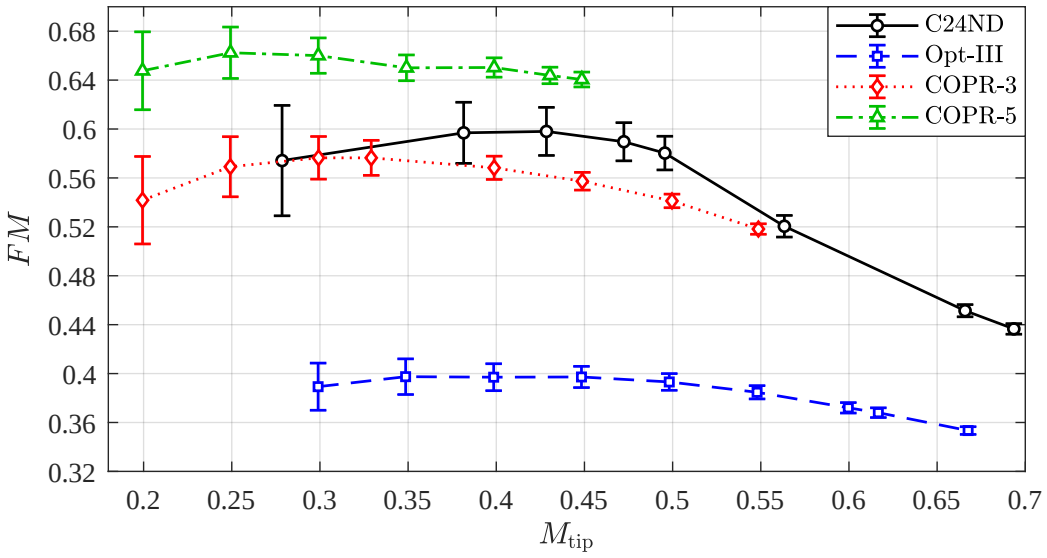

(a)

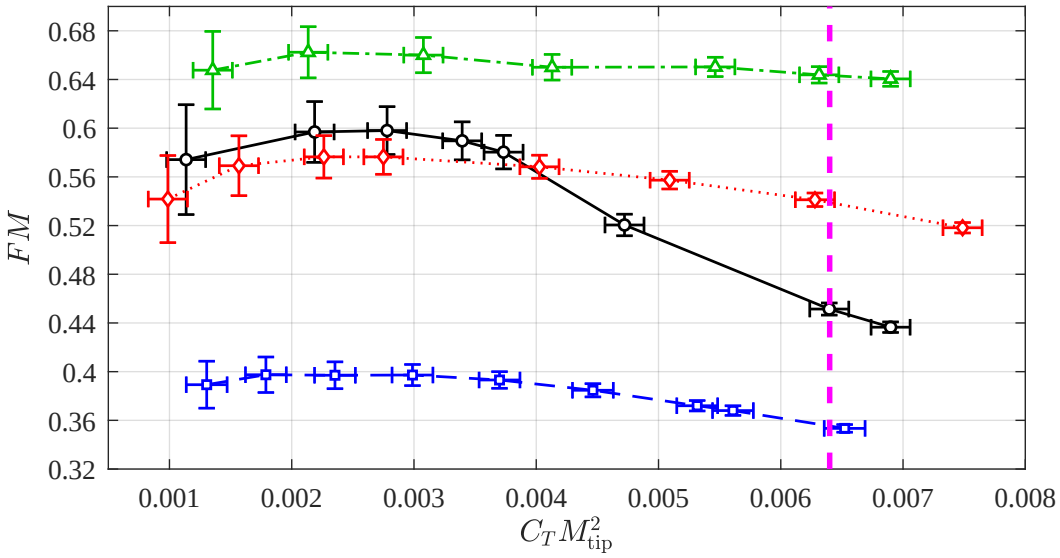

(b)

Figure 19. Figure of Merit for the tested proprotors plotted against (a) tip Mach number and (b) thrust setting. *Note: target hover thrust setting denoted by '- - -' in (b).*

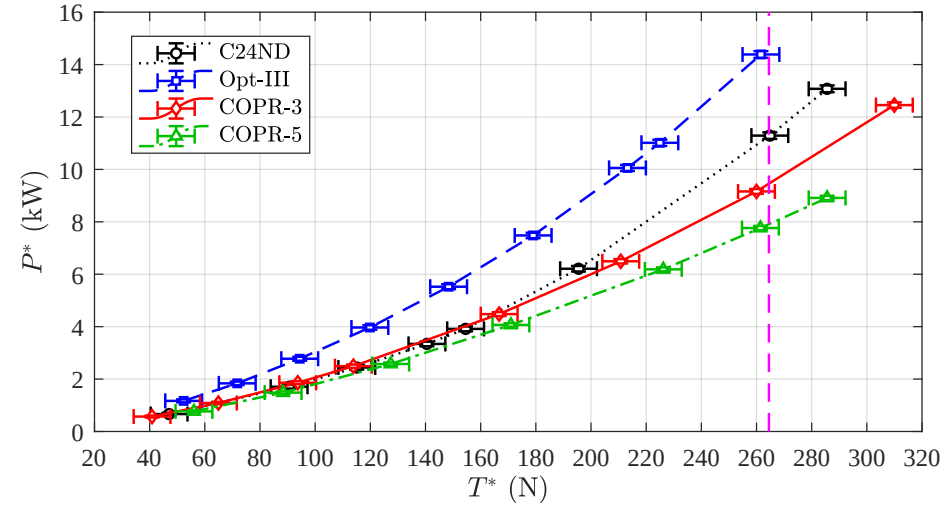

(a)

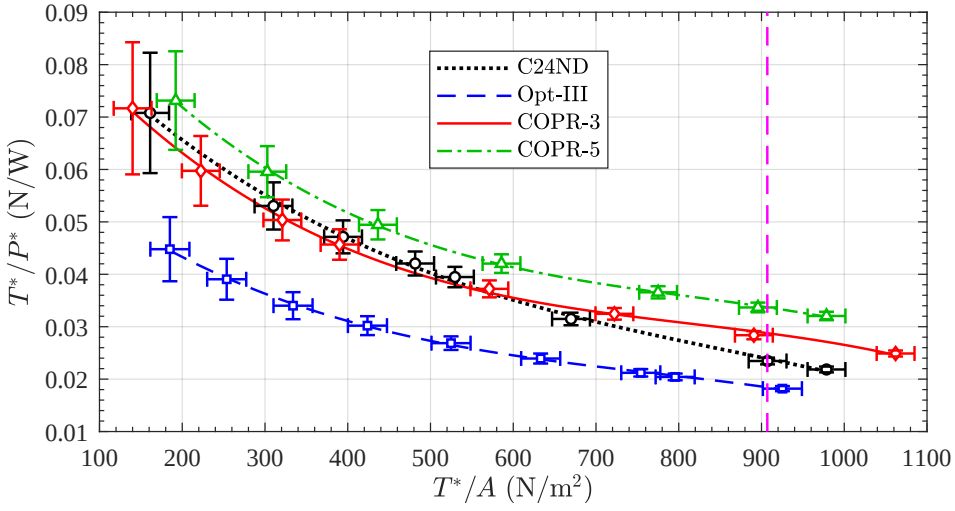

(b)

Figure 20. Dimensional (a) power-thrust profiles and (b) power loading vs. disk loading profiles for tested proprotors in static hover conditions. *Note: target hover thrust condition denoted by '- - -'; third order polynomial curve fits plotted with experimental run data in (b).*

5 Acoustic Performance

The acoustic characteristics of the four tested proprotors are discussed in this section. First, the proprotor acoustics in forward flight will be discussed, followed by hover acoustics. Each of these sections will present data in the form of narrowband acoustic spectra, averaged revolution acoustic pressure time histories, and extracted tonal and broadband directivities.

5.1 Forward Flight Acoustics

Figures 21 - 24 provide a narrowband spectral survey of the four proprotors at the target cruise condition across a range of shear-layer-corrected observers (see Appendix A) that span the LSAWT microphone array. All spectra plots include a measurement of the wind tunnel background noise, with no proprotor in operation. These data are computed utilizing the method 1 processing technique discussed in Section 3.3.2. Also included with each figure are the SLSD equivalent proprotor rotation rates and BPF, which are defined as

$$\Omega_{SLSD} = \Omega_m \frac{c_{SLSD}}{c_m}, \tag{20}$$

and

$$BPF^* = \Omega_{SLSD} \frac{N_b}{60}, \tag{21}$$

respectively. Note that Ω_m and c_m represent the proprotor rotation rate and atmospheric speed of sound measured during the experimental run, and N_b is the number of proprotor blades. The form of Eq. 21 assumes that Ω is expressed in units of revolutions per minute (RPM).

The spectra for the C24ND propeller in Fig. 21 reveal prominent tonal acoustic energy at all observers, with the strongest tonal energy present near the plane of the propeller ($\theta_c = 90°$). The first ten BPF harmonics are visible at $\theta_c = 90°$, and these harmonics are seen to greatly diminish in amplitude with increasing distance away from the propeller plane, for both increasing and decreasing observer angles. There is also a consistent flatband presence of broadband acoustic energy up to approximately 60 kHz, after which a sharp roll-off is observed.

Figure 22 shows the narrowband spectra for the Opt-III proprotor in cruise. These spectra reveal an overall reduction in both the tonal and broadband acoustic levels when compared to the C24ND results shown in Fig. 21. The higher BPF harmonics are both lower in amplitude and are seen to roll off at a faster rate for a given observer location. The BPF itself, however, is seen to have less of a difference between the two proprotors. The broadband noise content for the Opt-III proprotor is also seen to roll off more gradually with increasing frequency, as opposed to the near flatband appearance of the C24ND spectra.

Figure 23 shows the narrowband acoustic spectra survey data for the COPR-3 proprotor at the design cruise condition. It is worth observing that the higher harmonic content for this proprotor is negligible relative to the Opt-III and C24ND proprotors. This is because of the dramatically reduced tip speed condition at which this proprotor operates. Due to the considerably larger blade area (and thus blade

solidity), the thrust requirement of each blade per unit area is more relaxed, and the blade is a more efficient thrust generator. The COPR-3 is also seen to exhibit a dramatic reduction in broadband noise, with it being only slightly above the facility background noise.

Figure 24 shows the narrowband acoustic survey results for the COPR-5 proprotor at the cruise condition. Similar to the COPR-3, the broadband noise is only slightly above the facility background noise, and is actually lower than that of the COPR-3. This is believed to be due to the fact that the angles of attack experienced by the blades are reduced relative to the COPR-3, because the thrust condition remains constant, and the increased blade count reduces the thrust generated per blade. Since the blades have a common collective pitch setting between the two proprotors, this translates to reduced angles of attack. As a result of this, it is reasonable to expect that turbulent boundary layer separation near the trailing edges of the blade is reduced on the COPR-5 proprotor. This yields reduced blade self-noise. Regarding tonal noise, there are indications of the BPF in the spectral plots, however at only several dB above the facility background noise. Furthermore, while there is higher frequency tonal content in the spectra, it is relatively low in amplitude.

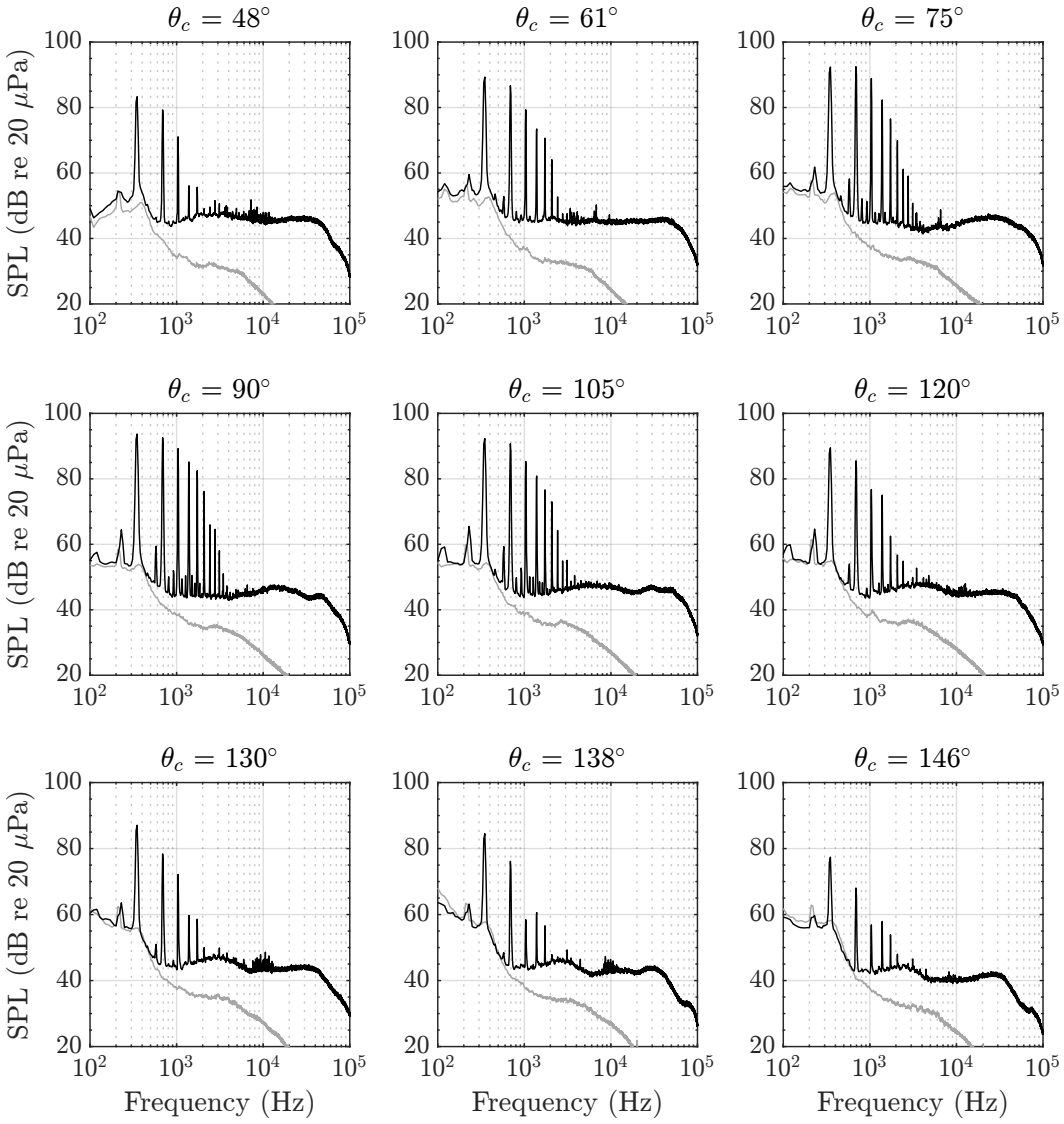

Figure 21. Narrowband acoustic spectra of the C24ND baseline propeller at design forward flight (cruise) condition at a series of corrected observer angles along the LSAWT linear microphone array. *Note: gray lines represent tunnel background noise (no propeller in operation) at M_∞ = 0.111; proprotor BPF* = 353 Hz, Ω_{SLSD} =* 7060 *RPM.*

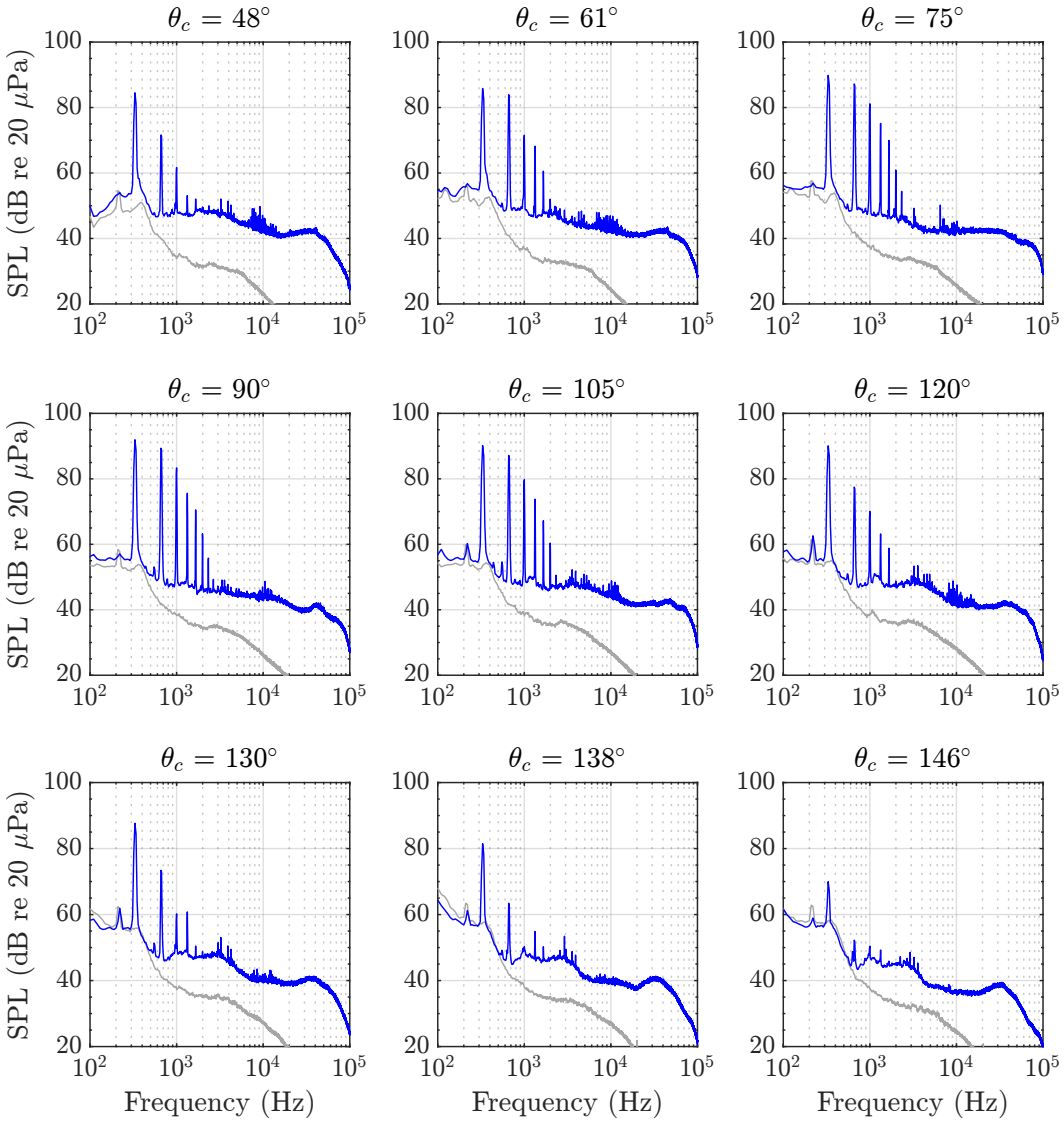

Figure 22. Narrowband acoustic spectra of the Opt-III proprotor at design forward flight (cruise) condition at a series of corrected observer angles along the LSAWT linear microphone array. *Note: gray lines represent tunnel background noise (no propeller in operation) at M_∞ = 0.111; proprotor BPF* = 334 Hz, Ω_{SLSD} = 6680 RPM.*

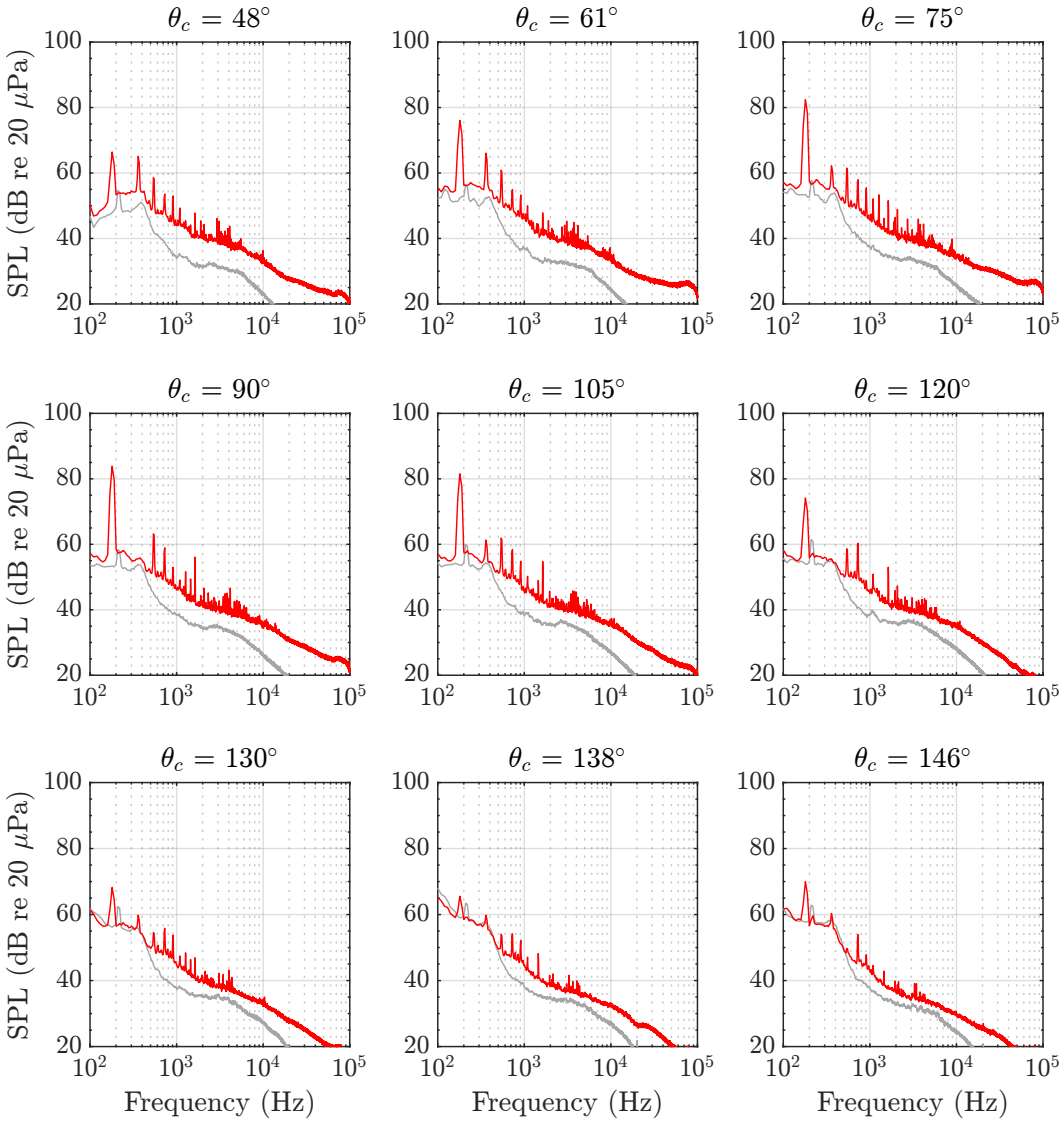

Figure 23. Narrowband acoustic spectra of the COPR-3 proprotor at design forward flight (cruise) condition at a series of corrected observer angles along the LSAWT linear microphone array. *Note: gray lines represent tunnel background noise (no propeller in operation) at $M_\infty = 0.111$; proprotor $BPF^* = 182$ Hz, $\Omega_{SLSD} = 3640$ RPM.*

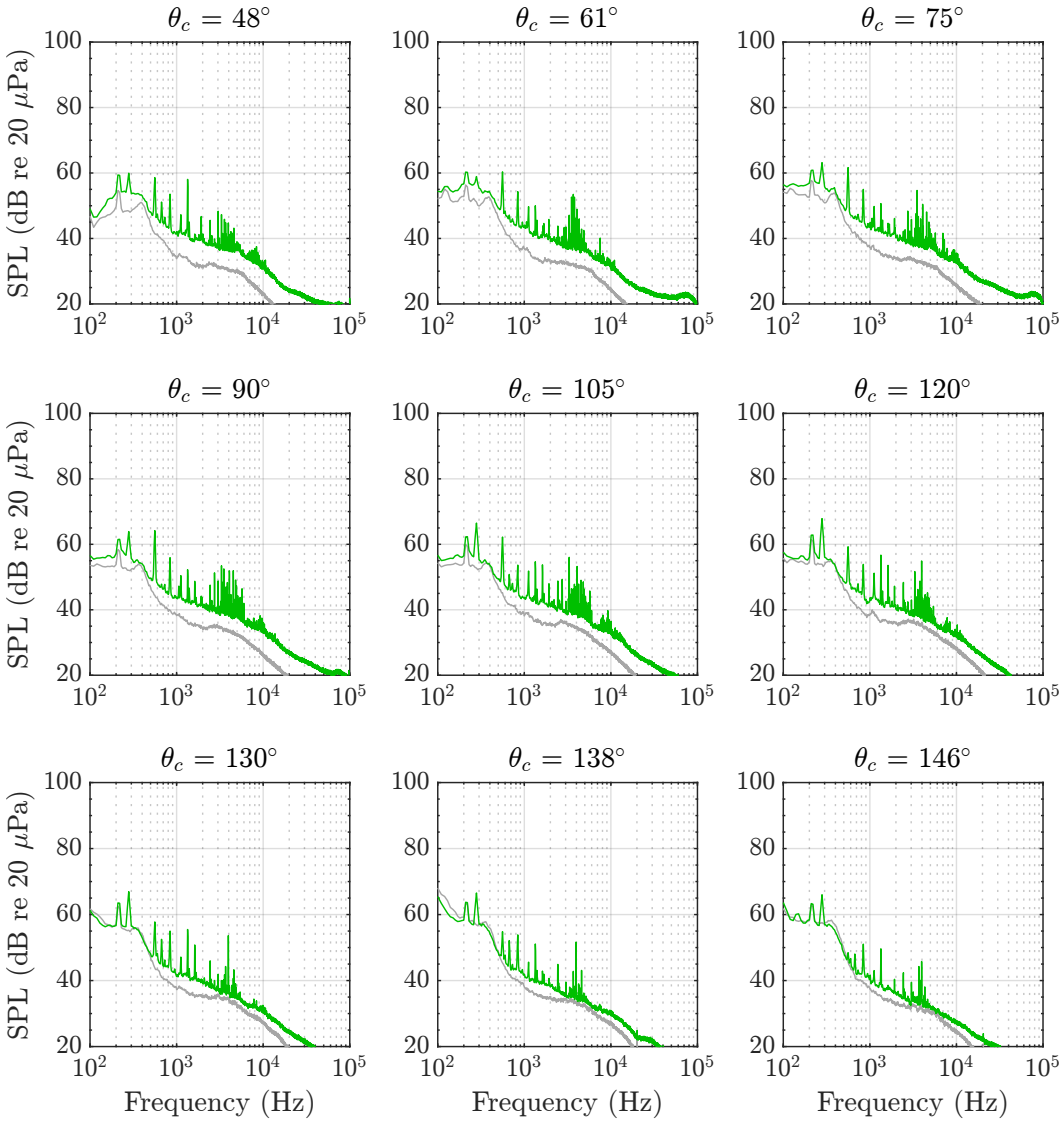

Figure 24. Narrowband acoustic spectra of the COPR-5 proprotor at design forward flight (cruise) condition at a series of corrected observer angles along the LSAWT linear microphone array. *Note: gray lines represent tunnel background noise (no propeller in operation) at $M_\infty = 0.111$; proprotor $BPF^* = 283$ Hz, $\Omega_{SLSD} = 3396$ RPM.*

Figure 25 provides the periodically averaged acoustic pressure time histories of all four proprotors along the LSAWT microphone array for the design cruise condition. Note that the data in this figure are computed using processing method 2 discussed in Section 3.3.2. The time histories are normalized by the revolution periods of each respective proprotor. These plots show a gradual increase in periodic energy as one approaches the plane of the proprotor, from either the upstream or downstream direction. The COPR-5, however, exhibits very low tonal levels relative to the other three proprotors, and does not display this trend. More details of this can be seen in Figs. 26 - 29, which show the directivities of the first three BPF harmonics for each proprotor. These BPF harmonics are computed using processing method 3 discussed in Section 3.3.2.

Figures 26 and 27 show that the Opt-III exhibits reduced tonal levels relative to the C24ND propeller. This is most noticeable for the second and third BPF harmonics, with the fundamental BPF only decreasing over part of the observer range. Figures 28 and 29 meanwhile, show a dramatic drop in all tonal levels for the COPR-3 and COPR-5 proprotors, most noticeably in the second and third BPF harmonics. This is due to a combination of both dramatically reduced tip speeds as well as alleviated blade loading relative to the first two proprotors. Furthermore, the COPR-3 second BPF harmonic is seen to exhibit two pressure nulls along the LSAWT array. The exact cause of this is not known, however it could be related to variations in loading from one blade to the next, possibly due to slight variations in blade collective settings, mass distributions, blade deformations, or vibrations on the PTS. [23]

Figure 30 provides the directivity measurements of both the tonal (i.e., periodic) and residual (i.e., broadband) components of noise for all tested proprotors. Effectively, the results of Fig. 30(a) represent the RMS of the data in Fig. 25 with appropriate shear layer and atmospheric attenuation corrections applied. This figure shows that all optimized proprotors exhibit reduced tonal levels relative to the baseline C24ND, with the COPR-5 exhibiting the lowest tonal noise levels. For reference, interrogation of the microphone data at $\theta_c = 90°$ reveals a tonal OASPL reduction of approximately 3 dB for the Opt-III, 14 dB for the COPR-3, and 30 dB for the COPR-5. This trend continues when looking at the broadband noise directivities in Fig. 30(b), however with different levels of reduction. At the same observer location, broadband OASPL reductions of 4 dB for the Opt-III, 12.5 dB for the COPR-3, and 13.5 dB for the COPR-5 proprotors are computed. It is also worth noting the relative noise levels between these two figures: namely that, with the exception of COPR-5, all proprotors exhibit considerably higher tonal noise levels than their broadband counterparts across the majority of measured observer angles. This is typical of propellers in forward flight.

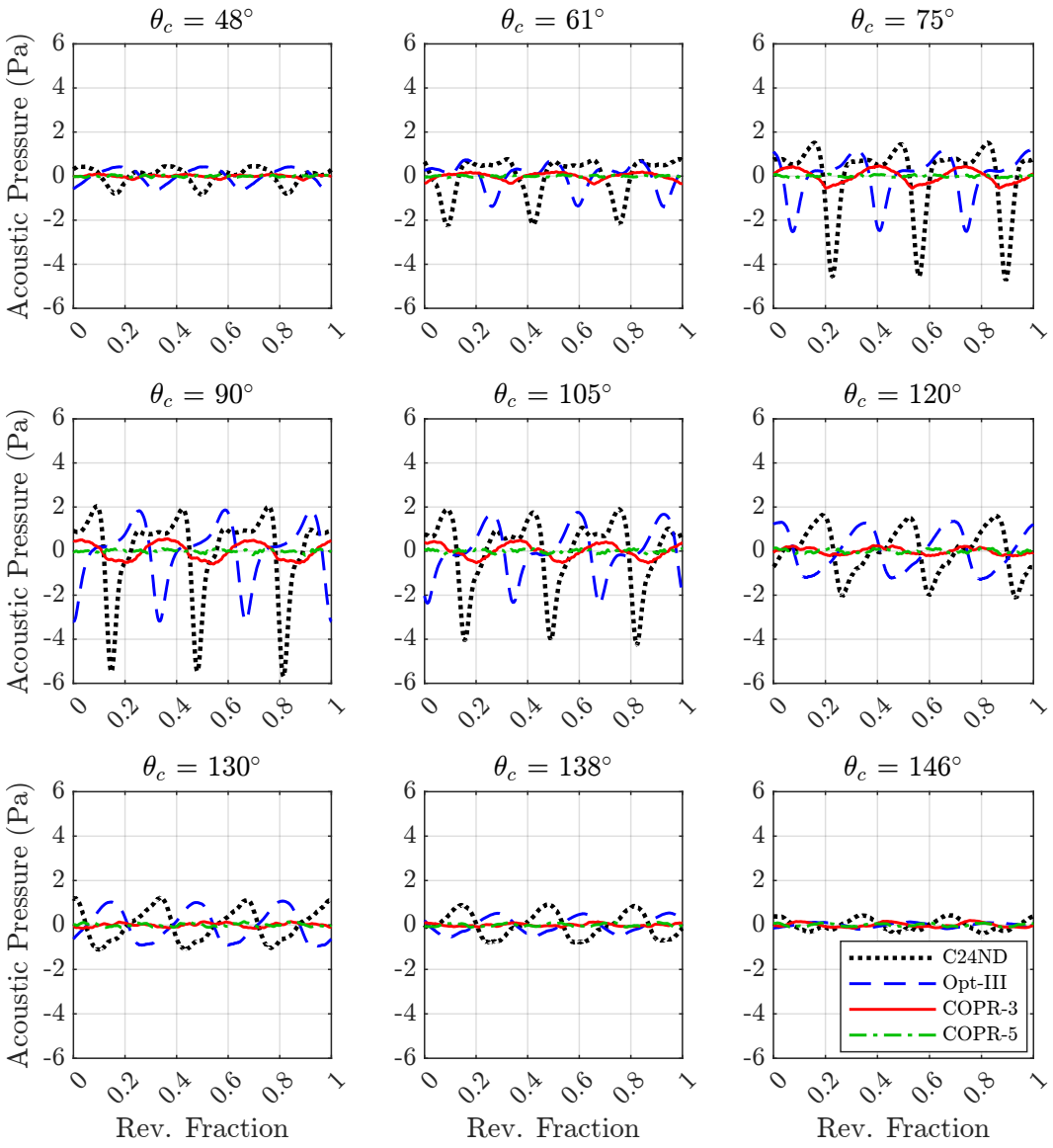

Figure 25. Periodically averaged acoustic pressure time histories of all tested proprotors at design forward flight (cruise) condition at a series of corrected observer angles along the LSAWT linear microphone array.

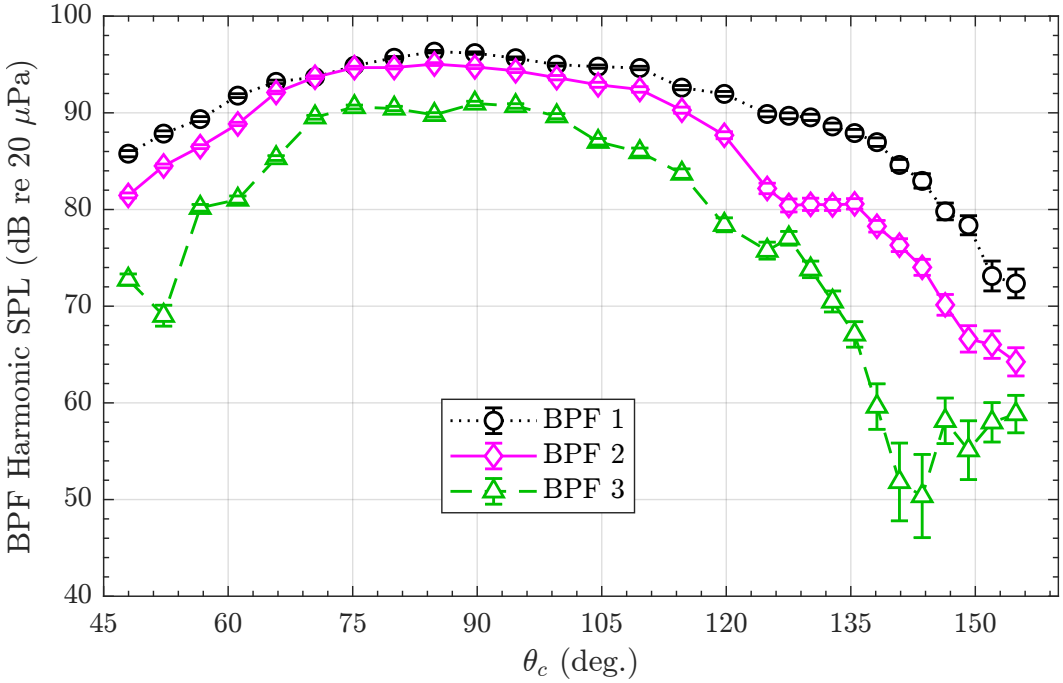

Figure 26. Extracted BPF harmonics for the C24ND propeller at design cruise condition. *Note: First three BPF harmonics shown.*

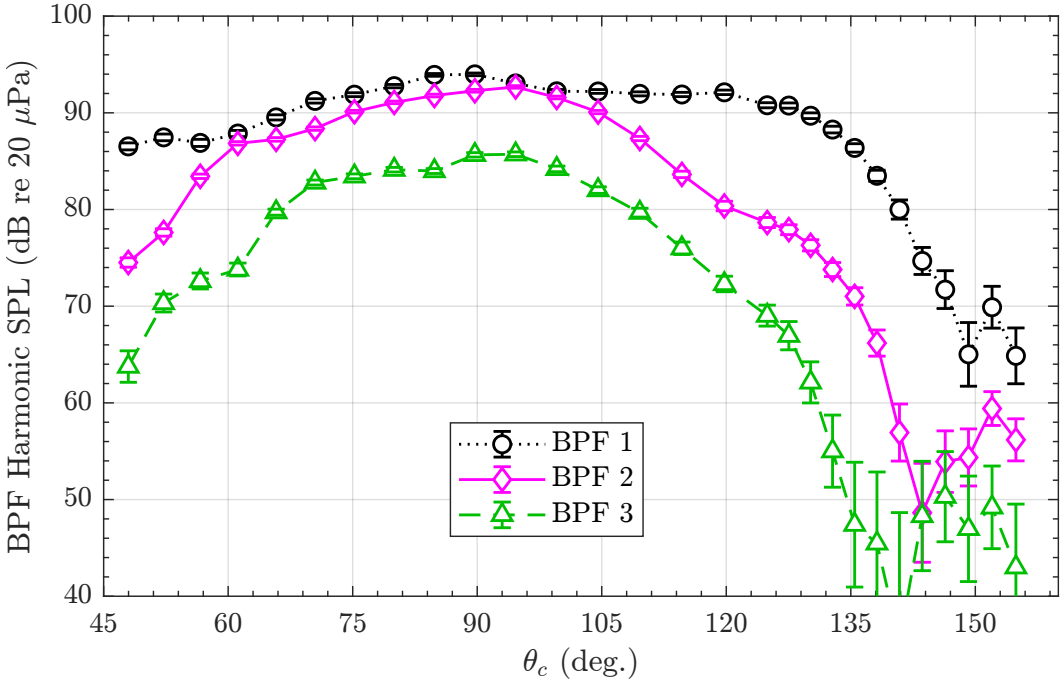

Figure 27. Extracted BPF harmonics for the Opt-III proprotor at design cruise condition. *Note: First three BPF harmonics shown.*

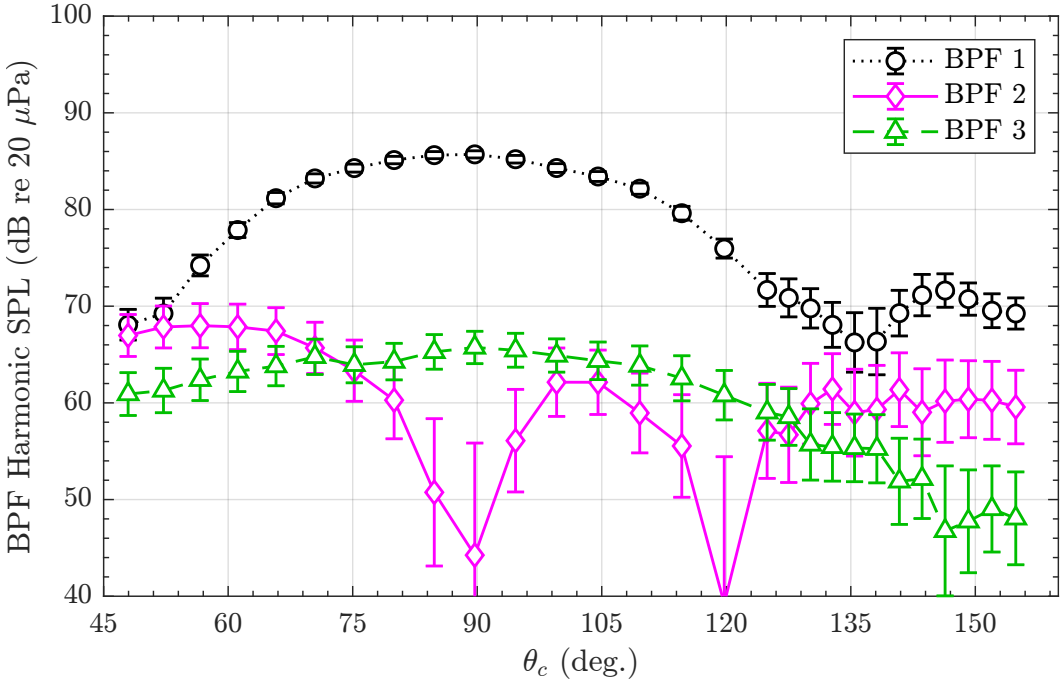

Figure 28. Extracted BPF harmonics for the COPR-3 proprotor at design cruise condition. *Note: First three BPF harmonics shown.*

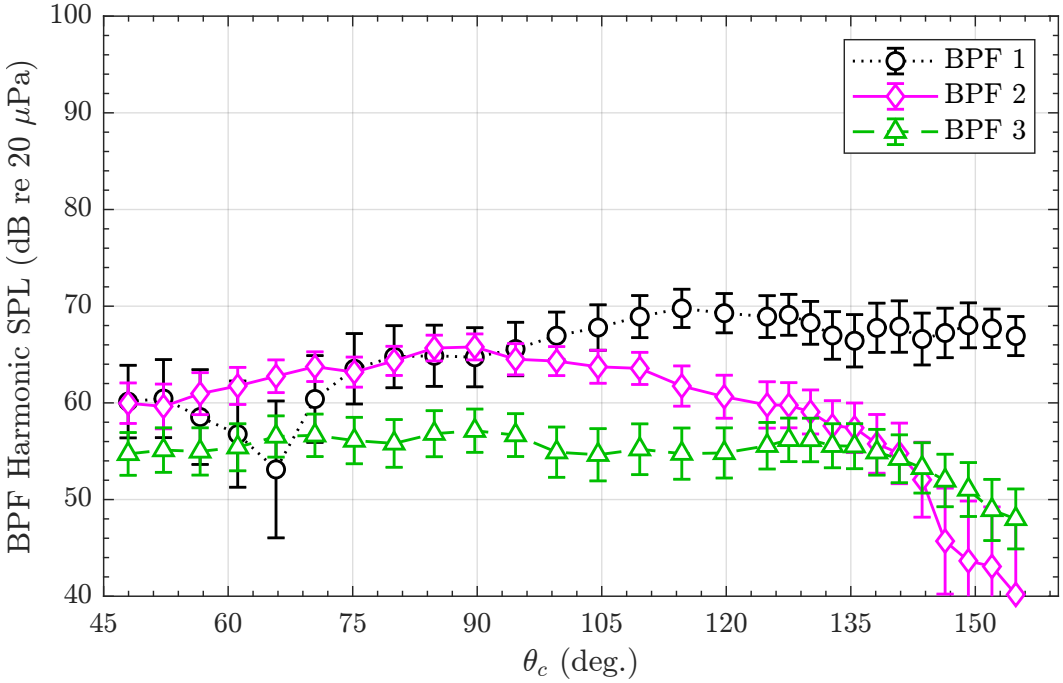

Figure 29. Extracted BPF harmonics for the COPR-5 proprotor at design cruise condition. *Note: First three BPF harmonics shown.*

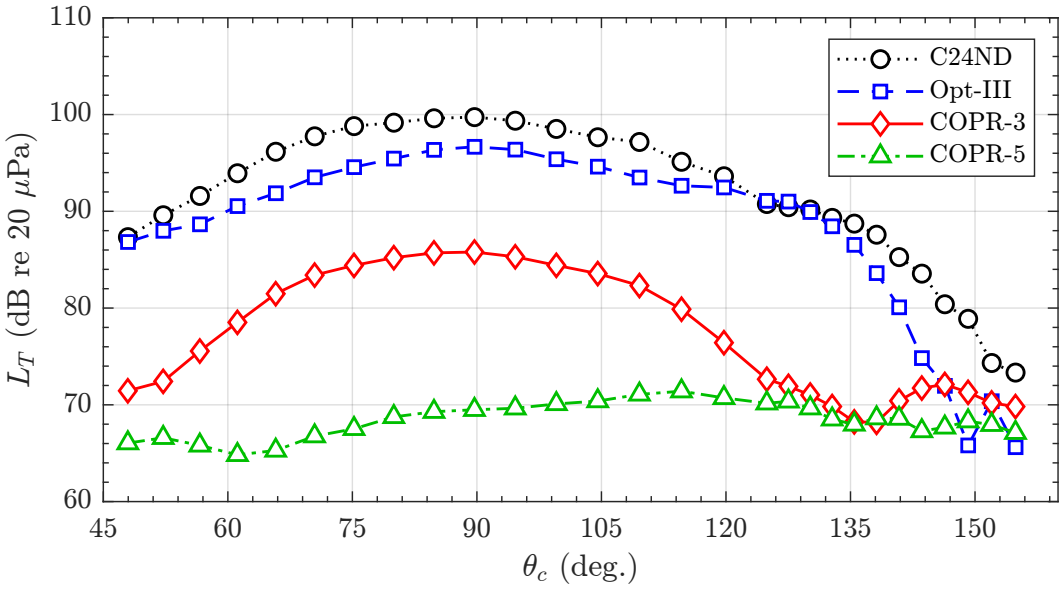

(a)

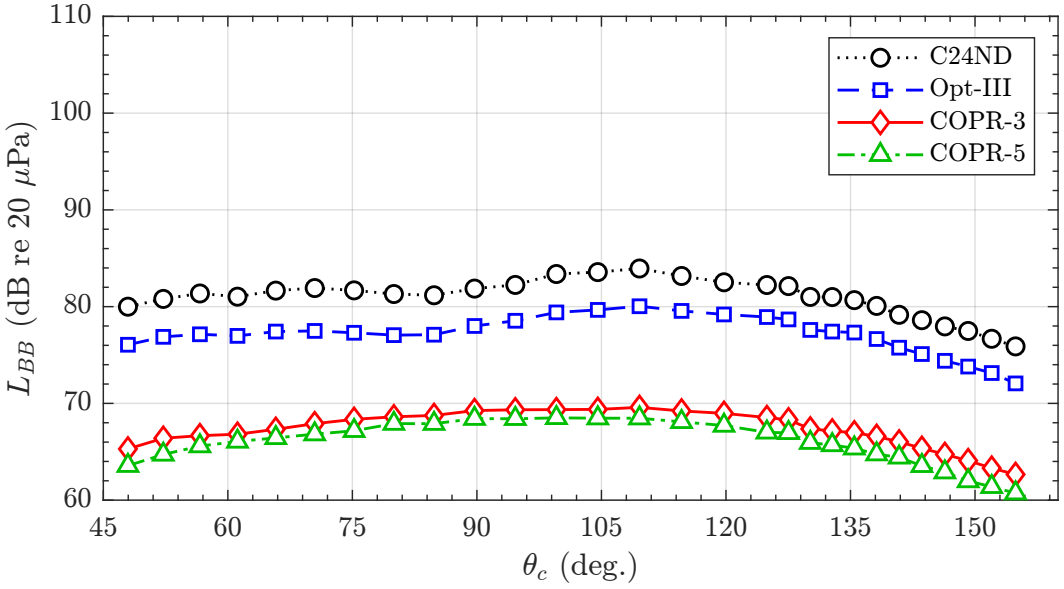

(b)

Figure 30. Directivities of (a) tonal and (b) broadband noise for all tested proprotors at target cruise condition.

5.2 Hover Acoustics

Figures 31 – 34 provide a narrowband spectral survey of the four proprotors in the target hover condition across a range of geometric observers, θ_o, that span the LSAWT microphone array. Note that these data are not shear-layer corrected due to the shear layer absence for the hover conditions. The spectra for the C24ND proprotor in Fig. 31 show prominent harmonic content across all observers. While some of this is due to the high blade loading of this flight condition, it may also be due to the excitation of the BPF harmonics due to turbulence ingestion and/or flow recirculation in the facility. This was discussed previously in Section 3.3.2. It is also worth noting the presence of harmonics at integer multiples of the proprotor rotation rate, in addition to those at integer multiples of the BPF. This is indicative of either mass imbalance and/or slight differences in pitch settings between the blades.

The Opt-III hover results of Fig. 32 are similar to those of the C24ND, however they show much less intermediate shaft harmonic content. This indicates that the Opt-III blades are better balanced than the C24ND ones. Also, there are slightly higher BPF harmonic amplitudes for the Opt-III, although with an overall reduction in high-frequency broadband noise.

The hover spectra for the COPR-3 proprotor in Fig. 33 show a shift in acoustic content to lower frequencies relative to the C24ND and Opt-III. This is due to the considerably lower rotation rate and thus tip speed for this proprotor. The COPR-5 results in Fig. 34 show a considerable reduction in both periodic and broadband acoustic levels relative to the COPR-3, as well as an increase in the frequencies of the BPF and associated harmonics. This is due to the increased blade count, and resulting lighter aerodynamic loading seen by each blade.

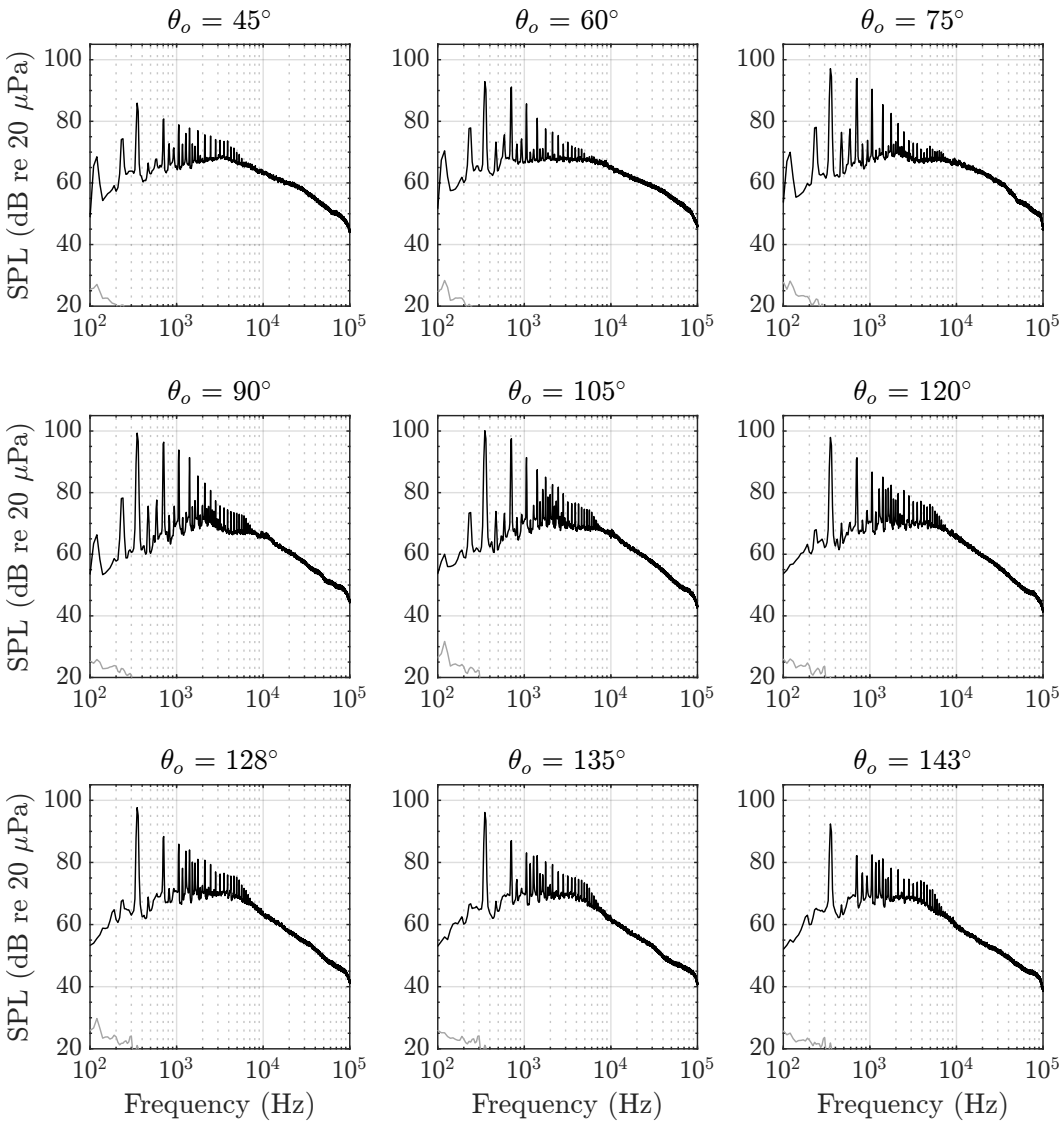

Figure 31. Narrowband acoustic spectra of the C24ND baseline propeller at design hover condition at a series of observer angles along the LSAWT linear microphone array. *Note: gray lines represent tunnel background noise (no propeller in operation) at static conditions; proprotor BPF* = 355 Hz,* $\Omega_{SLSD} = 7101$ *RPM.*

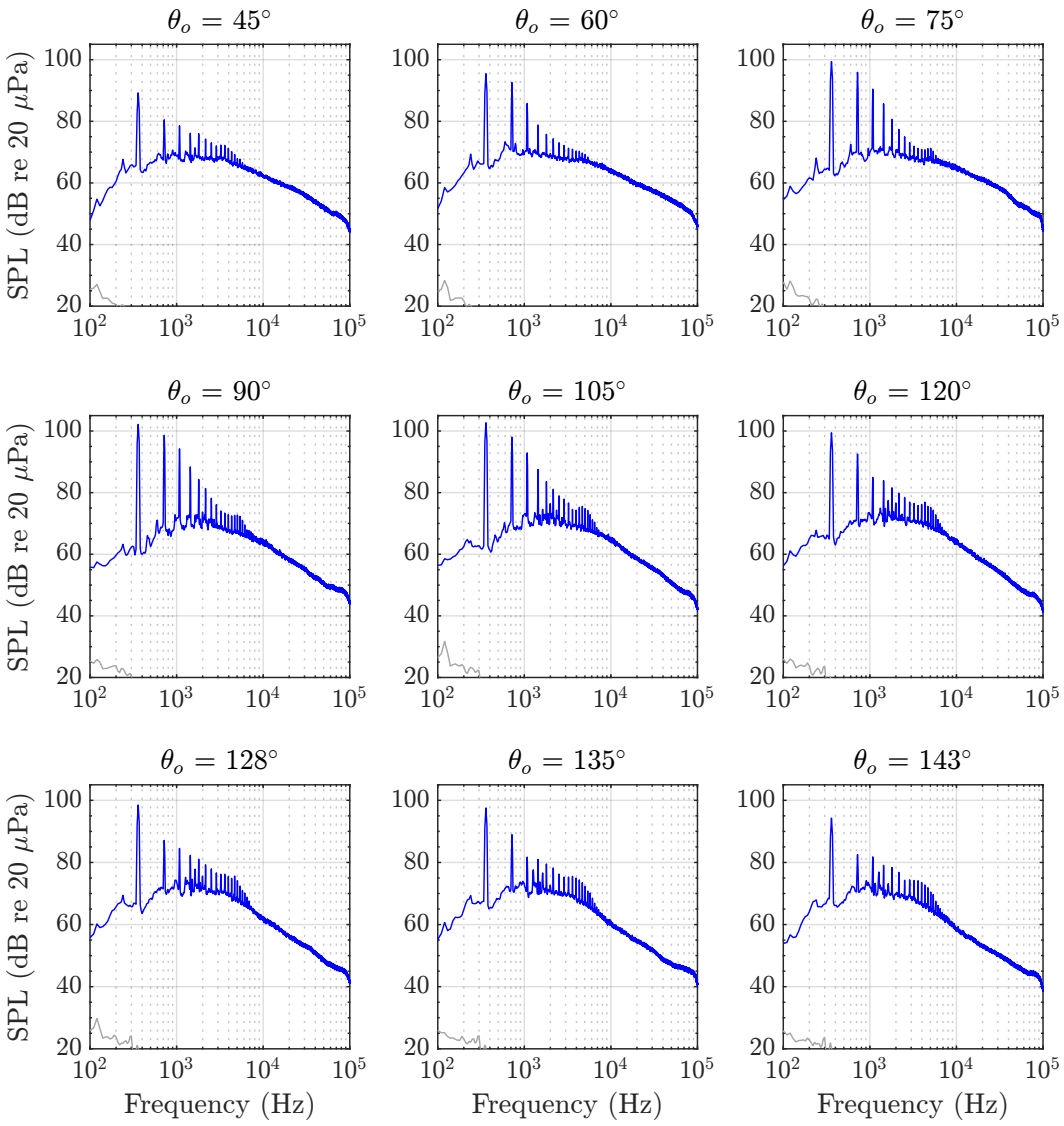

Figure 32. Narrowband acoustic spectra of the Opt-III proprotor at design hover condition at a series of observer angles along the LSAWT linear microphone array. *Note: gray lines represent tunnel background noise (no propeller in operation) at static conditions; proprotor* $BPF^* = 362$ *Hz,* $\Omega_{SLSD} = 7231$ *RPM.*

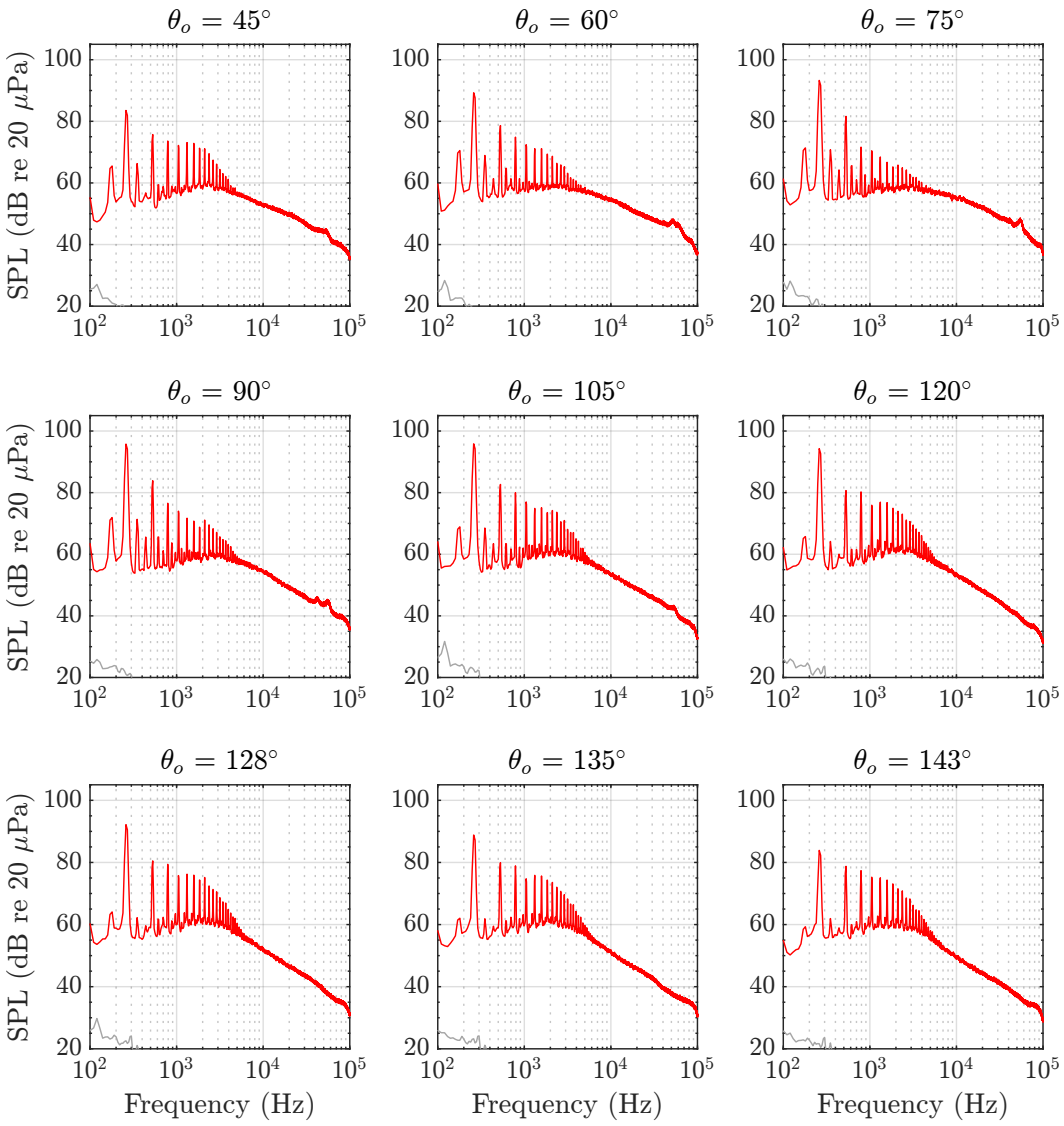

Figure 33. Narrowband acoustic spectra of the COPR-3 proprotor at design hover condition at a series of observer angles along the LSAWT linear microphone array. *Note: gray lines represent tunnel background noise (no propeller in operation) at static conditions; proprotor* $BPF^* = 266$ *Hz,* $\Omega_{SLSD} = 5330$ *RPM.*

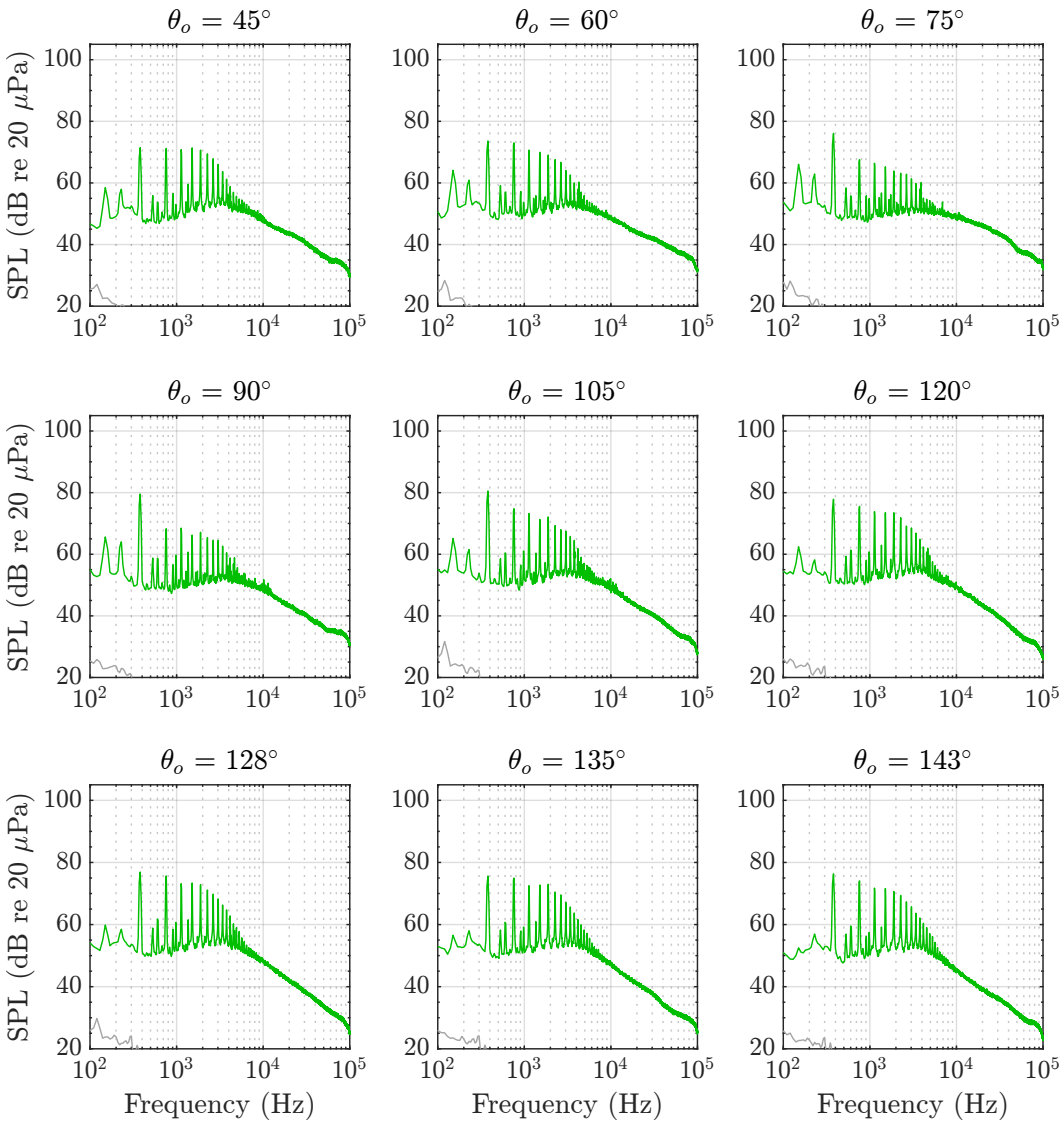

Figure 34. Narrowband acoustic spectra of the COPR-5 proprotor at design hover condition at a series of observer angles along the LSAWT linear microphone array. *Note: gray lines represent tunnel background noise (no propeller in operation) at static conditions; proprotor* $BPF^* = 382$ *Hz,* $\Omega_{SLSD} = 4590$ *RPM.*

Figure 35 shows the mean revolution acoustic pressure time histories for the tested proprotors in hover. These results show that the Opt-III exhibits higher tonal levels than the C24ND, particularly near the plane of the proprotor. This was unexpected since the Opt-III was designed to be quieter than the baseline for both cruise and hover conditions. It is worth noting that the tip speed of the Opt-III is also higher than the design condition, indicating that the proprotor needed to spin faster to generate the desired output thrust. This is most likely the result of flow separation and/or stall effects on the blade that were not accurately predicted. Furthermore, the COPR-3 shows a less impulsive waveform near the plane of the proprotor, however it is still of prominent amplitude. The COPR-5, meanwhile, shows a periodic waveform of considerably reduced amplitude, with the five blade passages most noticeable near the plane of the proprotor. This is again due to the fact that this intense loading condition is distributed over five blades instead of three.

Figures 36 – 39 show the directivities of the first three periodic extracted BPF harmonics for the tested proprotors. Comparison of Figs. 36 and 37 reveal that the most noticeably higher amplitude tone exhibited by the Opt-III relative to the C24ND is the fundamental BPF. This is most likely due to increased thickness noise associated with the higher rotation rate of the Opt-III. Figure 38 shows that the COPR-3 has reduced harmonic levels, relative to the two previous cases, also with higher uncertainties associated with them. This is because the extracted periodic values are at or below the random counterpart of the acoustic signal. These uncertainties increase for the COPR-5 in Fig. 39, where the periodic extracted harmonics are well below the raw measurement.

Figure 40 provides the directivities of the extracted periodic and broadband noise for the four tested proprotors in hover. The main difference that can be seen in these data relative to the cruise condition is that the broadband noise levels are comparable to their tonal counterparts. It is also worth noting that the COPR-5 is the only tested proprotor that exhibits broadband noise that is higher in level than the periodic noise. Furthermore, it is important to note that these "broadband" noise levels do retain a portion of the apparent harmonic acoustic energy, which is likely the result of aperiodic excitation of these harmonics due to turbulence ingestion. This was previously shown in Fig. 11. Contrary to expectations, the Opt-III actually exhibits a tonal OASPL that is 1.5 dB higher than the C24ND at an in-plane measurement location. The COPR-3 and COPR-5 proprotors, however, exhibit tonal noise reductions of 6 and 23 dB, respectively. As for broadband noise levels, the Opt-III, COPR-3, and COPR-5 proprotors exhibit in-plane OASPL reductions of 1.2 dB, 10 dB, and 16 dB, respectively.

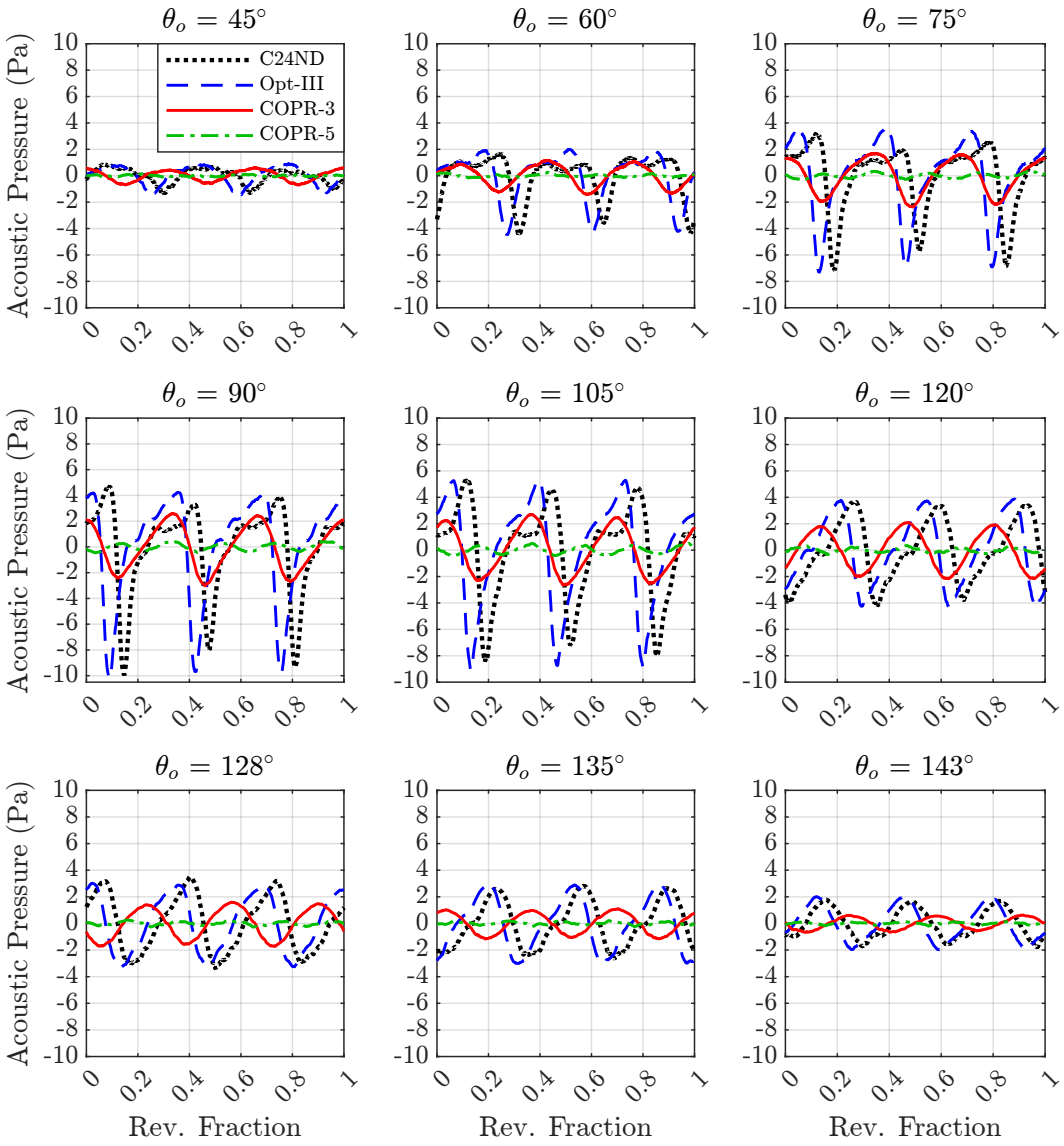

Figure 35. Periodically averaged acoustic pressure time histories of all tested proprotors at design hover condition at a series of observer angles along the LSAWT linear microphone array.

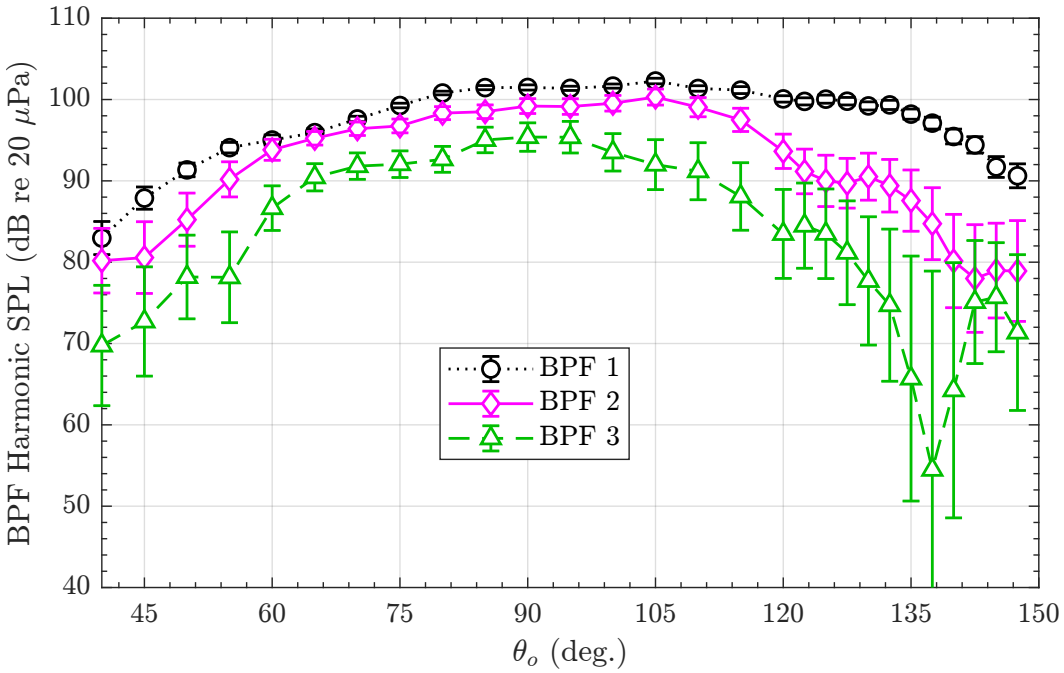

Figure 36. Extracted BPF harmonics for the C24ND propeller at design hover condition. *Note: First three BPF harmonics shown.*

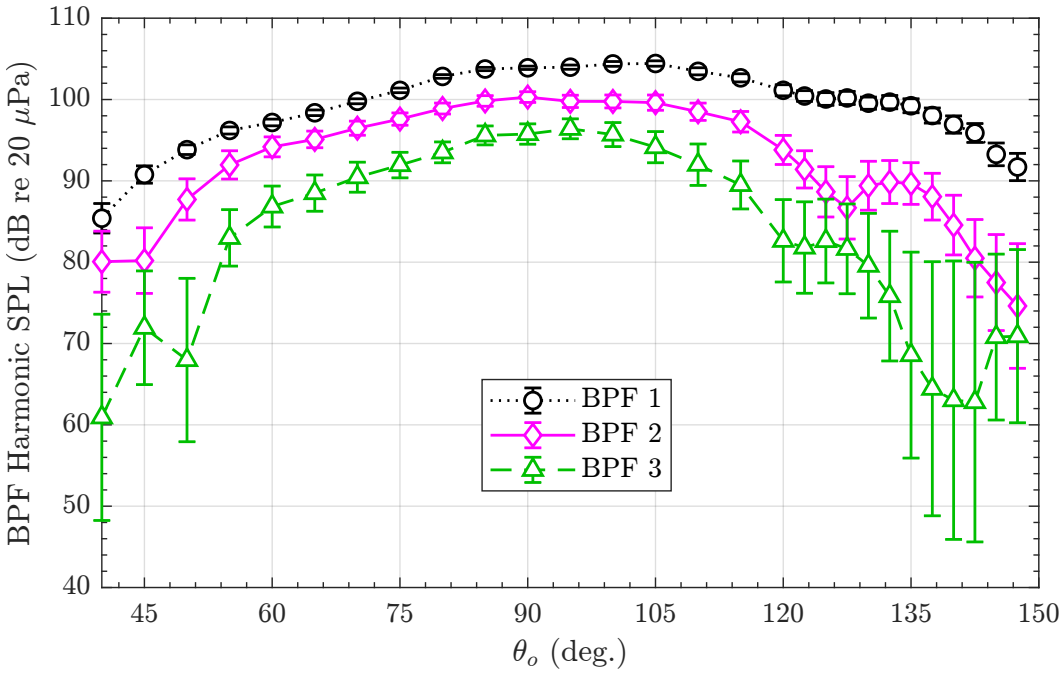

Figure 37. Extracted BPF harmonics for the Opt-III proprotor at design hover condition. *Note: First three BPF harmonics shown.*

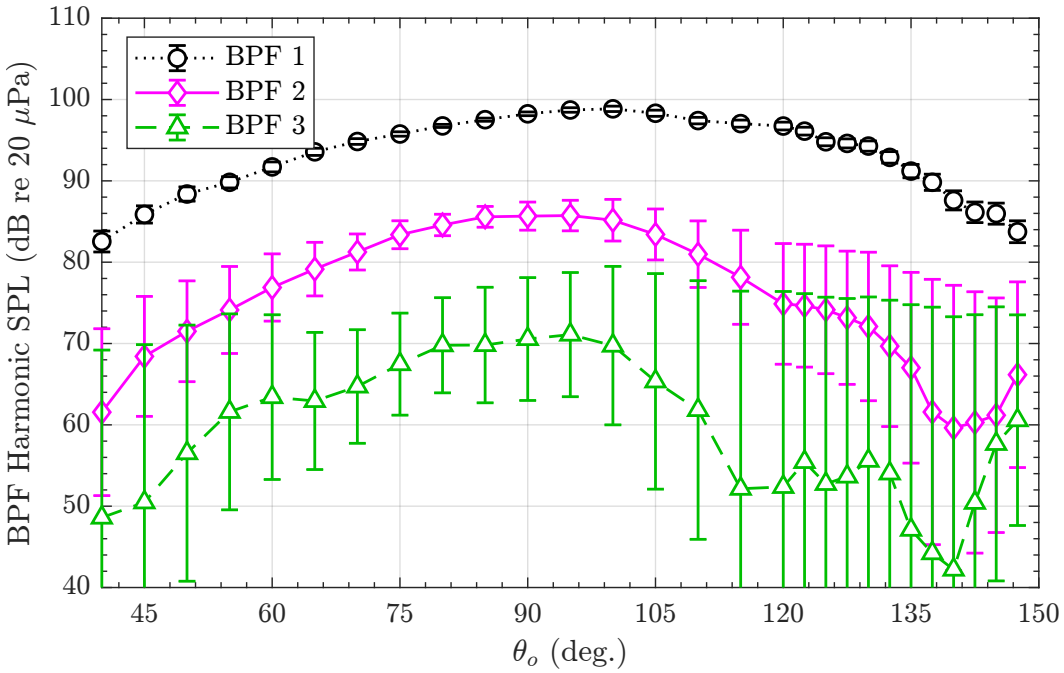

Figure 38. Extracted BPF harmonics for the COPR-3 proprotor at design hover condition. *Note: First three BPF harmonics shown.*

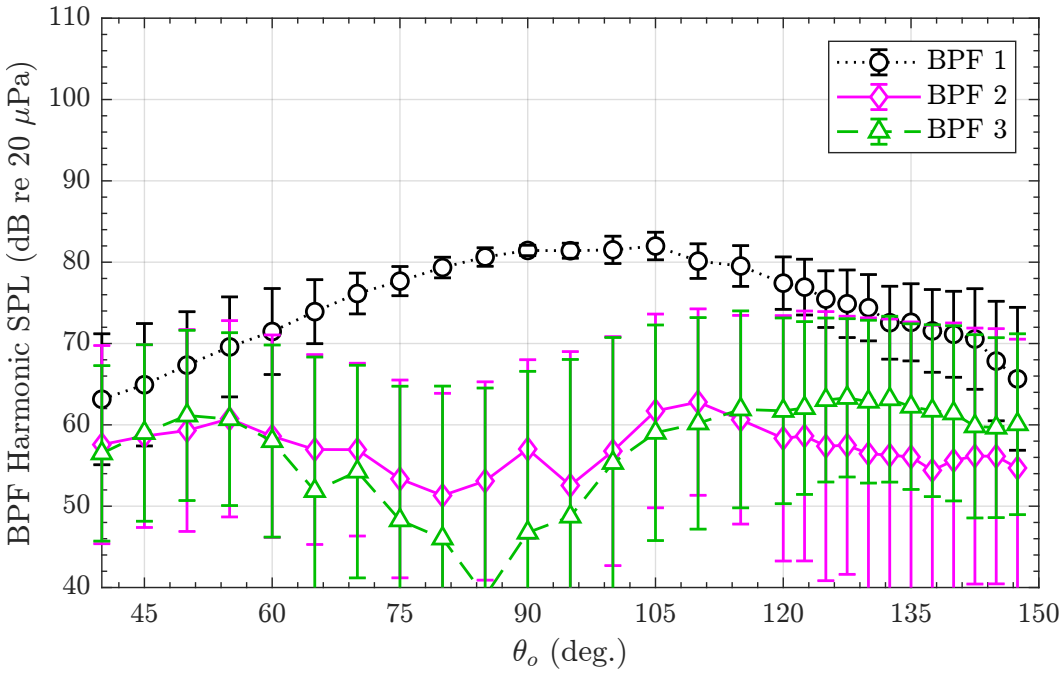

Figure 39. Extracted BPF harmonics for the COPR-5 proprotor at design hover condition. *Note: First three BPF harmonics shown.*

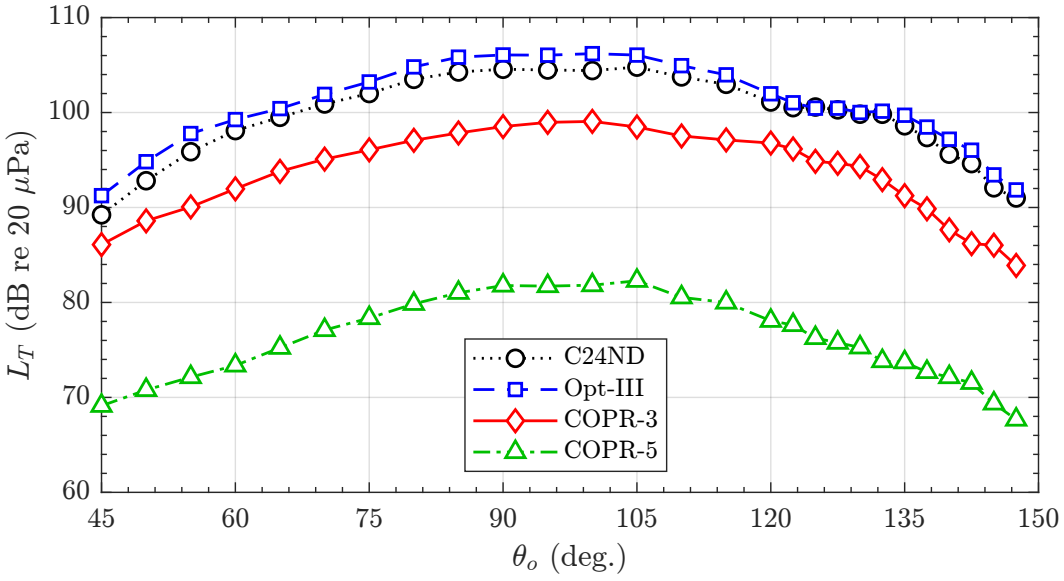

(a)

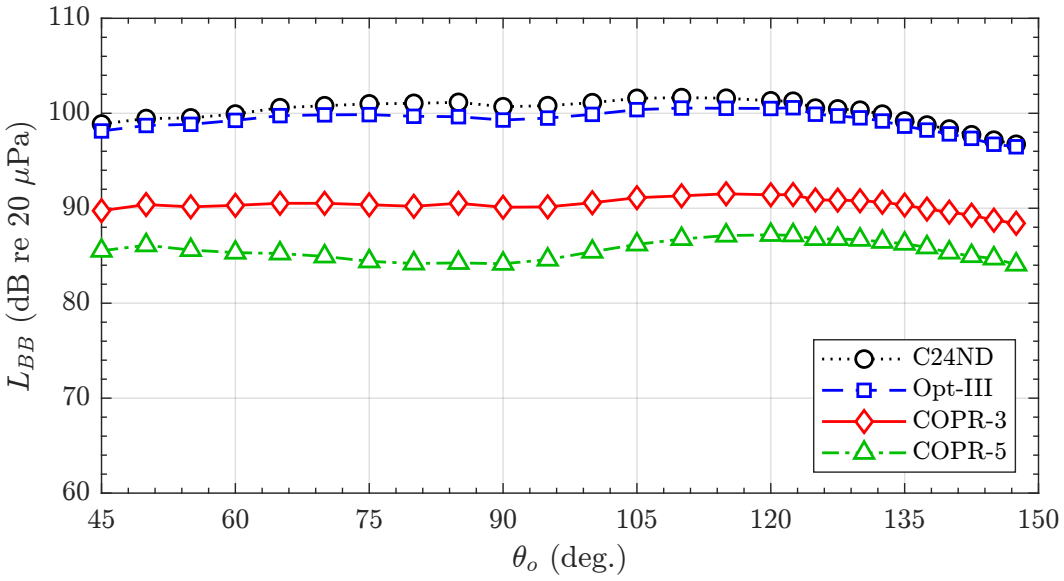

(b)

Figure 40. Directivities of (a) tonal and (b) broadband noise for all tested proprotors at target hover condition.

6 Conclusions and Future Work

An experimental test campaign was conducted in the NASA Langley LSAWT to measure the aerodynamic performance and acoustic characteristics of a series of proprotors for UAM applications. The flight conditions of interest included an axial forward flight condition representative of a propeller in cruise and a hover condition

representative of a rotor in VTOL. A helically twisted propeller geometry (C24ND) was used as a baseline design on which a high- and low-fidelity optimization was performed with the goal of outputting a proprotor design capable of performing comparably aerodynamically, with the goal of tonal noise minimization. Results show that tonal noise reduction was achieved in axial forward flight using both high- and low-fidelity optimization methods, with the low-fidelity optimization method performing considerably better. Specifically, a 3 dB tonal OASPL reduction was achieved at an in-plane observer for the high-fidelity optimized proprotor (Opt-III) in cruise, while a 14 dB tonal OASPL noise reduction was achieved for the low-fidelity optimized proprotor (COPR-3). A five-bladed version of the low-fidelity proprotor was also tested (COPR-5), and was found to yield a tonal OASPL noise reduction of 30 dB. In hover mode, however, only the COPR-3 and COPR-5 proprotors were found to exhibit tonal noise reductions. This is contrary to expectations because the Opt-III proprotor is the only design that underwent an acoustic optimization for the hover mode of flight. While capturing the aerodynamics in hover is a known challenge for high-fidelity computations, and was in this study, the chord length limitation of the high-fidelity computations of the Opt-III added another significant layer of complexity that challenged its ultimate design. While broadband noise was not considered in the noise optimization processes, all proprotor designs were found to exhibit broadband OASPL noise reductions in both flight conditions. However, the broadband OASPL reduction of the Opt-III in hover was rather modest at only 1.5 dB less than the C24ND levels.

A second installment of this documentation is planned, in which noise predictions will be compared with experimental measurements in an attempt to validate the proprotor designs. Both tonal and broadband predictions will be performed to help inform what aspects of noise generation were reduced, as well to help elucidate where the predictions and optimization routines are deficient.

7 References

1. Garrow, L. A., German, B., Schwab, N. T., Patterson, M. D., Mendonca, N., Gawdiak, Y. O. and Murphy, J. R., "A Proposed Taxonomy for Advanced Air Mobility," *AIAA AVIATION 2022 Forum*, AIAA Paper 2022-3321, Chicago, IL, June-July 2022.

2. Whiteside, S. K. S., Pollard, B. P., Antcliff, K. R., Zawodny, N. S., Fei, X., Silva, C., and Medina, G. L., "Design of a Tiltwing Concept Vehicle for Urban Air Mobility," Tech. Rep. NASA TM 20210017971, NASA Langley Research Center, Hampton, VA, United States, June 2021.

3. Farassat, F., "Linear Acoustic Formulas for Calculation of Rotating Blade Noise," *AIAA Journal*, Vol. 19, No. 9, Sep 1981, pp. 1122–1130.

4. Farassat, F. and Succi, G. P., "The prediction of helicopter rotor discrete frequency noise," *Proceedings of the 38th Annual Forum of the American Helicopter Society*, American Helicopter Society, Anaheim, CA, May 1982.

5. Farassat, F., "Derivation of Formulations 1 and 1A of Farassat," Tech. Rep. NASA TM 2007-214853, NASA Langley Research Center, Hampton, VA, United States, March 2007.

6. Ning, A., "Using blade element momentum methods with gradient-based design optimization," *Structural and Multidisciplinary Optimization*, Vol. 64, 2021, pp. 991–1014.

7. Leishman, J. G., *Principles of helicopter aerodynamics*, Cambridge aerospace series, Cambridge University Press, Cambridge, New York, 2nd ed., 2006, OCLC: ocm61463625.

8. Lopes, L. V., "Compact Assumption Applied to the Monopole Term of Farassat's Formulation," *21st AIAA/CEAS Aeroacoustics Conference*, AIAA Paper 2015-2673, Dallas, TX, June 2015.

9. Lopes, L. V., "Compact Assumption Applied to Monopole Term of Farassat's Formulations," *Journal of Aircraft*, Vol. 54, No. 5, September-October 2017, pp. 1649–1663.

10. Gray, J. S., Hearn, T. A., Moore, K. T., Hwang, J., Martins, J. and Ning, A., "Automatic Evaluation of Multidisciplinary Derivatives Using a Graph-Based Problem Formulation in OpenMDAO," *15th AIAA/ISSMO Multidisciplinary Analysis and Optimization Conference*, AIAA Paper 2014-2042, Atlanta, GA, June 2014.

11. Gill, P. E., Murray, W., and Saunders, M. A., "SNOPT: An SQP Algorithm for Large-Scale Constrained Optimization," *SIAM Review*, Vol. 47, No. 1, Jan 2005, pp. 99–131.

12. Wu, N., Kenway, G., Mader, C. A., Jasa, J. and Martins, J. R. R. A., "pyOptSparse: A Python framework for large-scale constrained nonlinear optimization of sparse systems," *The Journal of Open Source Software*, Vol. 5, No. 54, 2564, 2020.

13. Revels, J., Lubin, M., and Papamarkou, T., "Forward-Mode Automatic Differentiation in Julia," *arXiv:1607.07892 [cs.MS]*, 2016.

14. Ingraham, D., "Design Of A Low-Noise Propeller With Low-Order Tools," *NASA Acoustics Technical Working Group*, National Aeronautics and Space Administration, Virtual Event, April 2021.

15. Icke, R. Ö., Baysal, O, Lopes, L. V., and Diskin, B., "Optimizing Proprotor Blades Using Coupled Aeroacoustic and Aerodynamic Sensitivities," *AIAA AVIATION 2021 Forum*, AIAA Paper 2021-3037, Virtual Event, August 2021.

16. Zawodny, N. S. and Haskin, H. H., "Small Propeller and Rotor Testing Capabilities of the NASA Langley Low Speed Aeroacoustic Wind Tunnel," *23rd AIAA/CEAS Aeroacoustics Conference*, AIAA Paper 2017-3709. Denver, CO, June 2017.

17. Zawodny, N. S., Boyd, Jr., D. D. and Burley, C. L., "Acoustic Characterization and Prediction of Representative, Small-Scale Rotary-Wing Unmanned Aircraft System Components," *AHS International* 72$^{\text{nd}}$ *Annual Forum*, West Palm Beach, FL, May 2016.

18. Zawodny, N. S. and Pettingill, N. A., "Acoustic Wind Tunnel Measurements of a Quadcopter in Hover and Forward Flight Conditions," *Inter-Noise 2018*, pp. 487-500. Chicago, IL, August 2018.

19. Zawodny, N. S. and Boyd, Jr., D. D., "Investigation of Rotor-Airframe Interaction Noise Associated with Small-Scale Rotary-Wing Unmanned Aircraft Systems," *Journal of the American Helicopter Society*, Vol. 65, No. 1, 2020, pp. 1–18.

20. Bendat, J. S. and Piersol, A. G., *Random Data Analysis and Measurement Procedures*, chap. 9: Statistical Errors in Advanced Estimates, John Wiley & Sons Inc., 3rd ed., 2000, pp. 316–348.

21. Weitsman, D., Stephenson, J. H., and Zawodny, N. S., "Effects of flow recirculation on acoustic and dynamic measurements of rotary-wing systems operating in closed anechoic chambers," *The Journal of the Acoustical Society of America*, Vol. 148, No. 3, 2020, pp. 1325–1336.

22. Amiet, R. K., "Refraction of Sound by a Shear Layer," *Journal of Sound and Vibration*, Vol. 58, No. 4, 1978, pp. 467–482.

23. Zawodny, N. S., Haskin, H. H. and Nark, D. M., "Aerodynamic Performance and Acoustic Measurements of a High-Lift Propeller in an Isolated Configuration," *24th AIAA/CEAS Aeroacoustics Conference*, AIAA Paper 2018-3448, Atlanta, GA, June 2018.

Appendix A

LSAWT Microphone Array Shear Layer Corrections

Table A4 lists the geometric and shear layer-corrected locations and level corrections for the LSAWT linear microphone array. These are computed using the calculation method of Ref. [22] for a cylindrical shear layer and an equivalent "inflow" set of observers. These corrections are applied to all BPF harmonic, tonal OASPL, and broadband OASPL directivity plots presented in Section 5.1. Shear layer corrections are not applicable to computed hover data.

Table A4. LSAWT linear microphone array shear layer corrections ($M_\infty = 0.111$).

r_m, m	θ_o (deg.)	r_c, m	θ_c (deg.)	ΔdB_c	$\Delta\text{dB}_{r_c/r_{LSAWT}}$	$\Delta\text{dB}_\text{Total}$
5.50	40.00	5.07	47.97	1.36	0.55	1.91
5.00	45.00	4.64	52.23	1.26	0.32	1.58
4.62	50.00	4.32	56.64	1.16	0.16	1.32
4.32	55.00	4.07	61.16	1.05	0.06	1.11
4.08	60.00	3.88	65.78	0.92	0.00	0.92
3.90	65.00	3.74	70.46	0.79	-0.04	0.76
3.76	70.00	3.64	75.21	0.66	-0.05	0.60
3.66	75.00	3.57	80.00	0.51	-0.05	0.46
3.59	80.00	3.53	84.84	0.36	-0.04	0.32
3.55	85.00	3.53	89.71	0.21	-0.03	0.18
3.54	90.00	3.55	94.63	0.05	0.00	0.05
3.55	95.00	3.59	99.58	-0.11	0.02	-0.09
3.59	100.00	3.67	104.56	-0.26	0.04	-0.22
3.66	105.00	3.78	109.59	-0.41	0.06	-0.36
3.76	110.00	3.92	114.65	-0.56	0.06	-0.50
3.90	115.00	4.10	119.76	-0.70	0.05	-0.65
4.08	120.00	4.33	124.93	-0.83	0.03	-0.80
4.19	122.50	4.46	127.54	-0.89	0.00	-0.89
4.32	125.00	4.61	130.16	-0.94	-0.03	-0.97
4.46	127.50	4.78	132.80	-0.99	-0.07	-1.06
4.62	130.00	4.97	135.46	-1.03	-0.13	-1.16
4.80	132.50	5.18	138.15	-1.06	-0.20	-1.26
5.00	135.00	5.42	140.86	-1.08	-0.29	-1.37
5.24	137.50	5.69	143.60	-1.09	-0.40	-1.49
5.50	140.00	6.00	146.37	-1.07	-0.54	-1.61
5.81	142.50	6.36	149.17	-1.03	-0.72	-1.74
6.17	145.00	6.76	152.01	-0.94	-0.94	-1.88
6.58	147.50	7.24	154.88	-0.79	-1.22	-2.02

REPORT DOCUMENTATION PAGE	Form Approved OMB No. 0704–0188

1. REPORT DATE *(DD-MM-YYYY)*	2. REPORT TYPE	3. DATES COVERED *(From - To)*
01-02-2023	Technical Memorandum	

4. TITLE AND SUBTITLE
Experimental Validation of an Acoustically and Aerodynamically Optimized UAM Proprotor
Part 1: Test Setup and Results

5a. CONTRACT NUMBER

5b. GRANT NUMBER

5c. PROGRAM ELEMENT NUMBER

6. AUTHOR(S)
Nikolas S. Zawodny, Nicole A. Pettingill, Leonard V. Lopes and Daniel J. Ingraham

5d. PROJECT NUMBER

5e. TASK NUMBER

5f. WORK UNIT NUMBER

7. PERFORMING ORGANIZATION NAME(S) AND ADDRESS(ES)
NASA Langley Research Center
Hampton, Virginia 23681-2199

8. PERFORMING ORGANIZATION REPORT NUMBER
L–12456

9. SPONSORING/MONITORING AGENCY NAME(S) AND ADDRESS(ES)
National Aeronautics and Space Administration
Washington, DC 20546-0001

10. SPONSOR/MONITOR'S ACRONYM(S)
NASA

11. SPONSOR/MONITOR'S REPORT NUMBER(S)
NASA/TM–20220015637

12. DISTRIBUTION/AVAILABILITY STATEMENT
Unclassified-Unlimited
Subject Category 64
Availability: NASA STI Program (757) 864-9658

13. SUPPLEMENTARY NOTES
An electronic version can be found at http://ntrs.nasa.gov.

14. ABSTRACT
Vehicles with vectored thrust capabilities are common configurations proposed for Urban Air Mobility (UAM) flight missions. These include proprotor systems capable of vertical takeoff and landing (VTOL), axial forward flight, and the intermediate transition phases of vehicle flight. The aerodynamic loading requirements, as well as resulting acoustics, during these different phases of flight can vary considerably. An optimization effort was undertaken with the objective of minimizing radiated tonal acoustics of a proprotor system for both static hover and axial forward flight conditions, while simultaneously preserving aerodynamic performance relative to a baseline propeller design.

15. SUBJECT TERMS
Proprotor, Urban Air Mobility, Acoustics

16. SECURITY CLASSIFICATION OF:			17. LIMITATION OF ABSTRACT	18. NUMBER OF PAGES	19a. NAME OF RESPONSIBLE PERSON
a. REPORT	b. ABSTRACT	c. THIS PAGE			STI Information Desk (help@sti.nasa.gov)
U	U	U	UU	64	19b. TELEPHONE NUMBER *(Include area code)* (757) 864-9658